PNAS RESEARCH ARTICLE | EARTH, ATMOSPHERIC, AND PLANETARY SCIENCES

Mantle oxidation by sulfur drives the formation of giant gold deposits in subduction zones

Deng-Yang He[a], Kun-Feng Qiu[a,b,1], Adam C. Simon[c], Gleb S. Pokrovski[b], Hao-Cheng Yu[a], James A. D. Connolly[d], Shan-Shan Li[e], Simon Turner[f], Qing-Fei Wang[a], Meng-Fan Yang[a], and Jun Deng[a,g,1]

Affiliations are included on p. 10.

Edited by Terry Plank, Columbia University, Palisades, NY; received March 7, 2024; accepted November 18, 2024

Oxidation of the sub-arc mantle driven by slab-derived fluids has been hypothesized to contribute to the formation of gold deposits in magmatic arc environments that host the majority of metal resources on Earth. However, the mechanism by which the infiltration of slab-derived fluids into the mantle wedge changes its oxidation state and affects Au enrichment remains poorly understood. Here, we present the results of a numerical model that demonstrates that slab-derived fluids introduce large amounts of sulfate (S^{6+}) into the overlying mantle wedge that increase its oxygen fugacity by up to 3 to 4 log units relative to the pristine mantle. Our model predicts that as much as 1 wt.% of the total dissolved sulfur in slab-derived fluids reacting with mantle rocks is present as the trisulfur radical ion, S_3^-. This sulfur ligand stabilizes the aqueous $Au(HS)S_3^-$ complex, which can transport Au concentrations of several grams per cubic meter of fluid. Such concentrations are more than three orders of magnitude higher than the average abundance of Au in the mantle. Our data thus demonstrate that an aqueous fluid phase can extract 10 to 100 times more Au than in a fluid-absent rock-melt system during mantle partial melting at redox conditions close to the sulfide-sulfate boundary. We conclude that oxidation by slab-derived fluids is the primary cause of Au mobility and enrichment in the mantle wedge and that aqueous fluid-assisted mantle melting is a prerequisite for formation of Au-rich magmatic hydrothermal and orogenic gold systems in subduction zone settings.

Significance

Upon subduction, the oceanic crust releases aqueous fluids that infiltrate the overlying mantle. Compared to primitive mantle, this metasomatized mantle is enriched in gold and other economic metals to provide a source for mineral deposits. However, the fundamental causes of metal enrichment remain enigmatic. We demonstrate that sulfur is the key agent causing Au enrichment in the fluid upon its reaction with the mantle, by forming the soluble $Au(HS)S_3^-$ complex. This species concentrates in fluid up to 1,000 times more Au than its average mantle abundance. This gold enrichment in fluid is a key condition for forming Au-rich melts by fluid-present mantle melting. Our work provides a quantitative assessment of the behaviors of sulfur and gold during subduction-related processes.

sulfur redox | oxygen fugacity | mantle wedge | gold deposits | subduction zone

Subduction zones are the main regions of mass exchange between the mantle and crust on Earth. In particular, metals, water, and other volatiles are transferred from the subducting slab to overlying mantle wedge by fluids (1–3) and melts (4, 5). These fluids and melts are considered to be oxidized relative to those from the pristine mantle beneath the mid-ocean ridges (6). Different arc magma geochemical signatures, such as elevated total boron concentrations and $\delta^{11}B$ values (7) along with enrichment in large-ion lithophile elements (8) mirror those of the subducted oceanic slab, suggesting a connection between mantle wedge oxidation and the input of slab-related components (6). Thus, metasomatized peridotite xenoliths from the sub-arc mantle record oxygen fugacity values up to 2 log units higher than those of the conventional fayalite-magnetite-quartz (FMQ) buffer [$\log(fO_2)$ from ΔFMQ–1 to ΔFMQ+2] (9–11). Such redox conditions support the hypothesis that slab-derived fluids oxidize the mantle wedge.

Because oxidized sulfur (S^{4+} and S^{6+}), present as sulfate and sulfite species (HSO_4^-, SO_4^{2-}, HSO_3^-, SO_2) and their ion pairs with major cations (Na, K, Ca, Mg), is believed to be soluble in high-pressure aqueous fluids, infiltration of such fluids may explain why the sub-arc mantle wedge would be oxidized relative to depleted mantle (12–15). The input of sulfate-bearing slab-derived fluids is also supported by elevated $\delta^{34}S$ values in arc lavas (16, 17). Oxidizing agents such as sulfate and ferric iron are thought to be required for resorption of Au-bearing sulfides during partial melting of the mantle wedge (11, 18, 19), making such oxidation phenomena essential for the formation of porphyry and orogenic gold deposits. However, compared to more reduced sulfur species such as HS^-, H_2S, and S_3^-, which are major sulfur ligands for transporting Au in aqueous fluids (20, 21), sulfate has little capacity to form Au complexes. Because of a lack of quantitative assessment of the impact of such sulfur-mediated redox reactions both on the oxidation state of the mantle wedge and gold solubility in aqueous fluids and silicate melts originating from the metasomatized mantle, it is unclear how these opposing factors can be reconciled to explain gold transport within the mantle wedge.

Here, we report the results of thermodynamic simulations that quantitatively predict the chemistry of fluids generated by prograde devolatilization of subducted oceanic crust. We show that the resulting sulfate-bearing fluids oxidize ferrous iron in the silicate minerals

Author contributions: D.-Y.H., K.-F.Q., and J.D. designed research; D.-Y.H., H.-C.Y., Q.-F.W., and M.-F.Y. performed research; G.S.P. and J.A.D.C. contributed new reagents/analytic tools; A.C.S., G.S.P., H.-C.Y., J.A.D.C., S.-S.L., S.T., and M.-F.Y. analyzed data; K.-F.Q., A.C.S., and G.S.P. fund application; J.D. acquired funding; and D.-Y.H., K.-F.Q., A.C.S., G.S.P., H.-C.Y., J.A.D.C., S.-S.L., S.T., Q.-F.W., M.-F.Y., and J.D. wrote the paper.

The authors declare no competing interest.

This article is a PNAS Direct Submission.

[1] To whom correspondence may be addressed. Email: kunfengqiu@qq.com or djun@cugb.edu.cn.

This article contains supporting information online at https://www.pnas.org/lookup/suppl/doi:10.1073/pnas.2404731121/-/DCSupplemental.

within the mantle wedge. As a consequence of this oxidation, the fluid becomes reduced and enriched in trisulfur radical ion, S_3^-, which forms soluble complexes such as $Au(HS)S_3^-$ with Au. We propose that this sulfur-driven redox phenomenon is the fundamental mechanism of Au enrichment in magmatic arcs that host a major proportion of global economic resources of gold. These findings highlight that mantle oxidation improves the recycling efficiency of volatiles and metals in subduction zones.

Results

Devolatilization of Altered Oceanic Crust and Sulfur Mobility. Results from the devolatilization models (see *Materials and Methods* below) of altered oceanic crust (AOC) reveal two dominant dehydration stages along hot (1,000 °C, 2.4 GPa) and cold (1,000 °C, 3.3 GPa) subduction geothermal gradients (Fig. 1). The dehydration of chlorite and talc occurs at temperatures (T) T < 575 °C with removal of ~20% of the total water contained in the hydrated AOC (Fig. 1 *A* and *B* and *SI Appendix*, Fig. S1). The second stage occurs at forearc to sub-arc depths of 60 to 80 km for warm subduction, and of 80 to 120 km for cold subduction. During this stage, ~75% of the initial water contained in the AOC is released through dehydration of epidote, lawsonite, pumpellyite, and stilpnomelane. Lawsonite and muscovite are predicted to carry the remaining ~5% of water in the AOC to the deep mantle (>120 km) in the cold subduction regime (Fig. 1*B*).

Our model predicts that about 60% and 90% of the initial sulfur in AOC is released from hot and cold subducting slabs, respectively, during the second stage of dehydration (*SI Appendix*, Fig. S1 *A* and *B*). Aqueous sulfur speciation evolves along the hot geotherm, transforming from dominantly reduced (HS^- and H_2S) in the first dehydration stage to dominantly oxidized (HSO_4^-, SO_4^{2-}, KSO_4^-, HSO_3^-, and SO_2) during the second dehydration stage (Fig. 1*C*). In contrast, fluid speciation along the cold geotherm is always dominated by sulfate with only minor H_2S, HS^- and SO_2 (Fig. 1*D*). For both hot and cold subduction geotherms, the majority of the S is released to the aqueous fluid when pyrite (S^-) is oxidized to anhydrite (S^{6+}) in the 475 to 600 °C range (Fig. 1 and *SI Appendix*, Fig. S2). Our model predicts an increase in the $Fe^{3+}/\Sigma Fe$ ratio of garnet and decrease in clinopyroxene and the bulk rock system, over the interval of pyrite oxidation to anhydrite, both for cold and hot subduction scenarios (*SI Appendix*, Figs. S1 and S2).

Oxidative Capacity of Slab-Derived Fluid. To evaluate the metasomatic effects induced by slab-derived fluids in hot and cold subduction zones, we calculated the change in oxygen fugacity

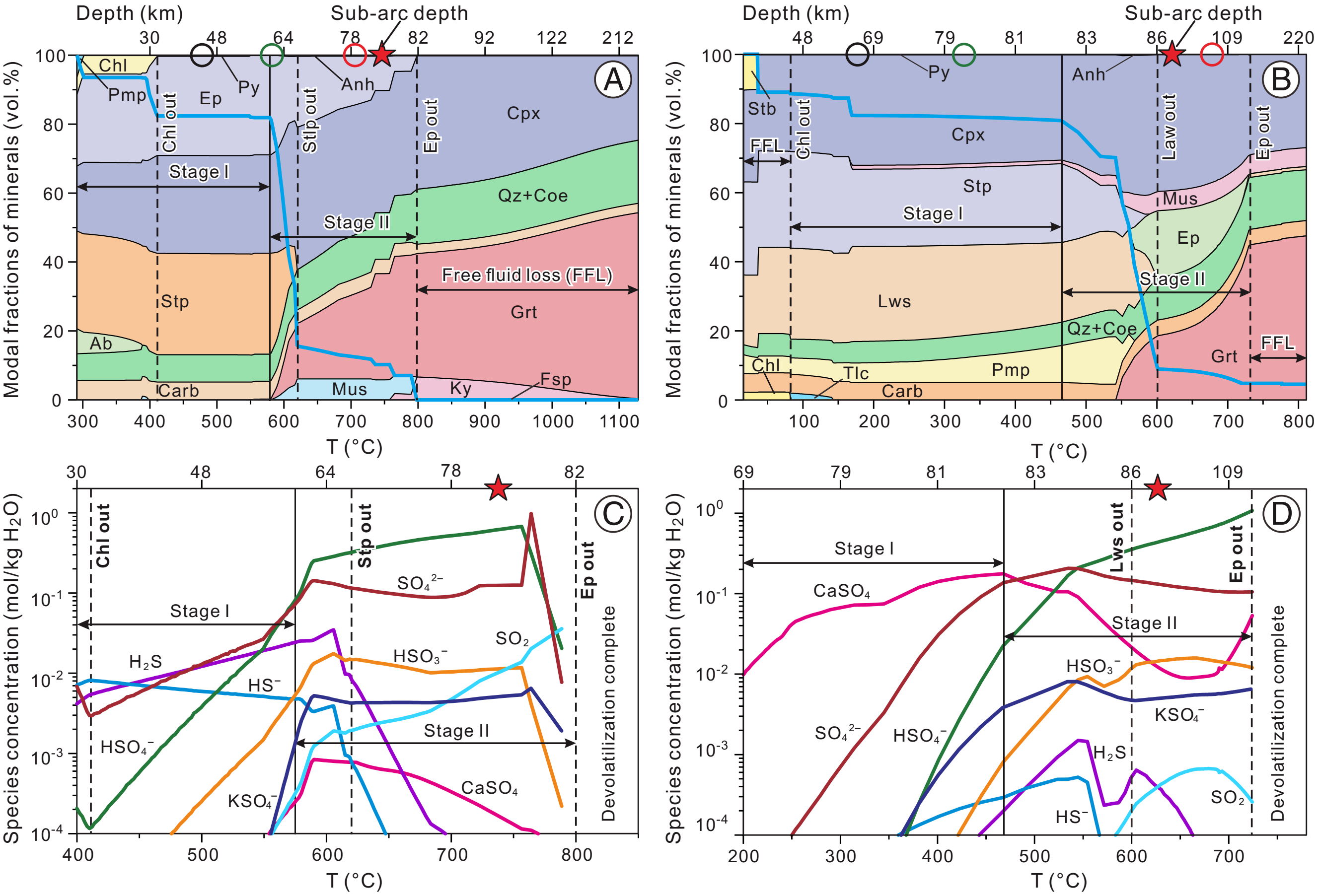

Fig. 1. Mineral assemblages and dominant sulfur species in the devolatilization fluid for an average AOC along the hot (central Cascadia) and cold (central Honshu) subduction pressure–temperature (P-T) paths. (*A* and *B*) Proportions (vol.%) of main minerals along the hot (*A*) and cold (*B*) subduction geotherms. (*C* and *D*) Molality (mol/kg H_2O) of dominant sulfur aqueous species along the hot (*C*) and cold (*D*) P-T paths. Temperature and corresponding slab depth are both plotted along the x-axis. The vertical black dash lines mark the complete breakdown of the dominant hydrous phases. Blue curves in (*A*) and (*B*) show the percentage of H_2O in solid hydrous phases. Red stars show the boundary depth between lithosphere and asthenosphere beneath the volcanic arc of a hot and cold subduction zone. Slab subduction P-T paths are from ref. 22. The black, green, and red open circles in (*A*) and (*B*) mark the extraction depths of fluids selected to compute the mantle infiltration model (*Materials and Methods*). The S_3^- ion is not shown in panels (*C* and *D*) because of its concentrations $<10^{-4}$ mol/kg H_2O, due to too oxidizing conditions of the slab devolatilization fluid. Mineral abbreviations: Ab–albite, Anh–anhydrite, Carb–carbonate, Chl–chlorite, Coe–coesite, Cpx–clinopyroxene, Ep–epidote, Grt–garnet, Ky–kyanite, Lws–lawsonite, Mus–muscovite, Fsp–feldspar, Pmp–pumpellyite, Py–pyrite, Qz–quartz, Stb–stilbite, Stp–stilpnomelane, Tlc–talc.

(fO_2) caused by the infiltration of fluids containing different S^{6+} concentrations (Fig. 2) into depleted mantle peridotite. For both hot and cold subduction geotherms, the interaction of mantle rocks with a fluid typically containing 1 to 2 wt.% S^{6+} increases the mantle fO_2 by at least two log units at plausible fluid/rock mass ratios (*R*) of 0.02 to 0.05 (Fig. 2 *A* and *B*, *Top* curves). In contrast, in both regimes, only a weak increase in fO_2 (0.2-0.5 log units) can be achieved by sulfur-poor (0.01-0.02 wt.% S) fluids and only at higher fluid/rock ratios ($R > 0.2$) (Fig. 2 *A* and *B*, *Bottom* curves). This difference demonstrates the importance of sulfur in the mantle oxidation process. Our model predicts that the mantle oxygen fugacity steeply increases during the initial infiltration of the S^{6+}-bearing fluid. With further fluid infiltration, the increase in fO_2 decreases (Fig. 2 *A* and *B*). A similar pattern is displayed in the $Fe^{3+}/\Sigma Fe$ ratio of garnet and pyroxene and X_{Mg} [Mg/(Mg+Fe)] values of olivine (*SI Appendix*, Fig. S3). These results demonstrate that the concentration of sulfate of the fluid plays a major role in the oxidation of the mantle wedge. In addition, the fluid infiltration model (see *Materials and Methods* below) predicts that pyrrhotite and pyrite are the dominant sulfide minerals for low to moderate degrees of metasomatism (i.e., low fluid/rock ratios, $R < 0.01$). With increasing fluid/rock ratio, Py + Anh and Pyh + Anh become the stable S-bearing mineral assemblages. The transition from Py + Anh to Pyh + Anh occurs at ~930 °C and ~1,050 °C for hot and cold subduction models, respectively (Fig. 3 *C* and *D*).

Sulfur and Gold Abundances and Chemical Speciation in Fluid Reacted with Mantle Wedge. The concentrations of sulfur species in slab-derived fluids after reaction with depleted mantle peridotite were computed for temperature of 1,000 °C and pressures of 2.4 and 3.3 GPa (Fig. 3 and *SI Appendix*, Figs. S4 and S5). At 2.4 GPa, in the presence of Py, Pyh, and Anh, elevated concentrations of sulfate

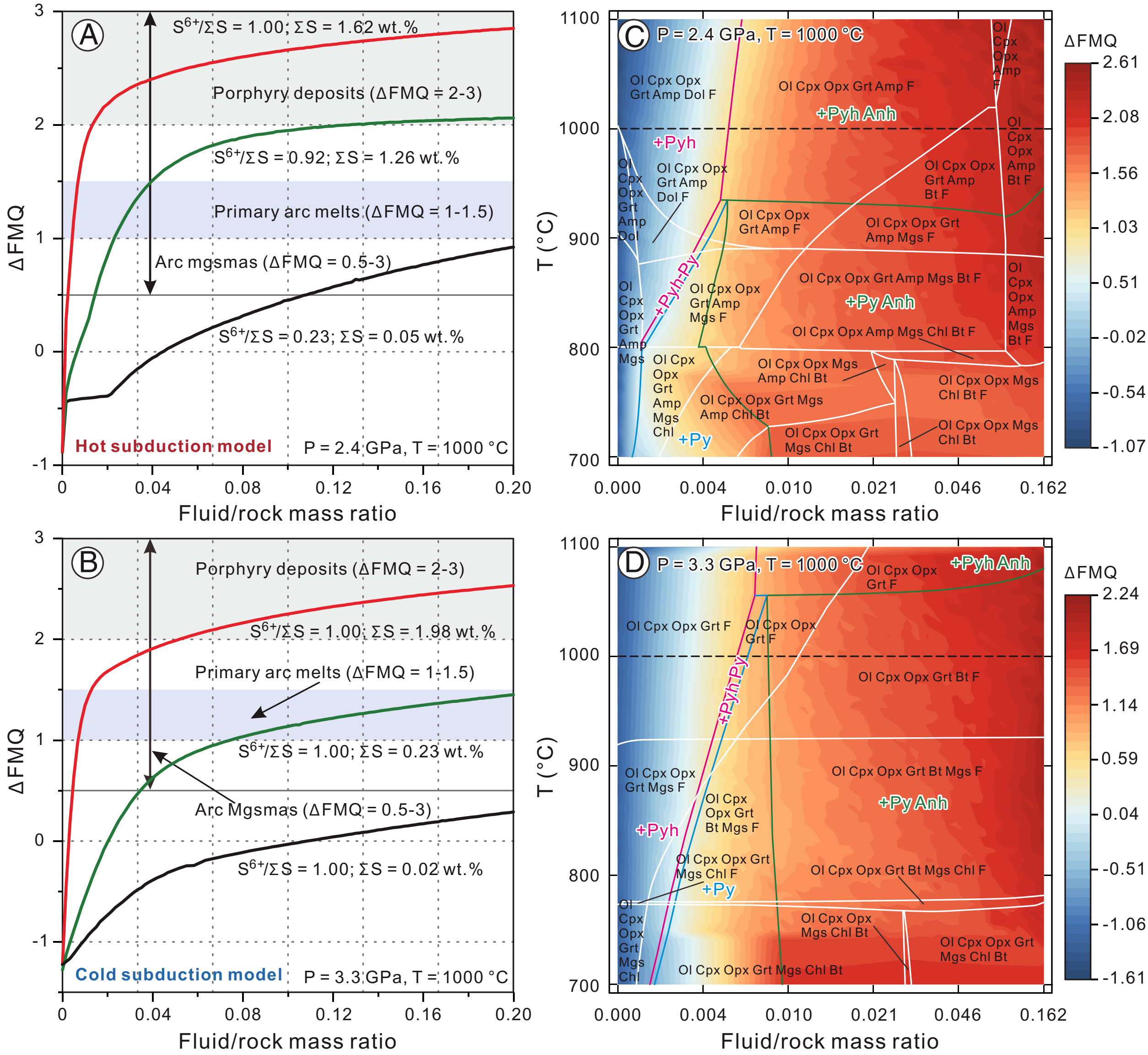

Fig. 2. Mantle wedge oxidation models showing the oxidation capacity of slab devolatilization fluids. (*A* and *B*) The capacity of aqueous fluid containing different S^{6+} concentrations to oxidize the mantle wedge at near wet-solidus conditions is computed for a hot (1,000 °C, 2.4 GPa) and a cold (1,000 °C, 3.3 GPa) subduction geotherm. (*C* and *D*) Variation of oxygen fugacity (color coded) and stable mineral assemblages for T = 700 to 1,100 °C and *P* = 2.4 and 3.3 GPa, computed by mixing depleted mantle peridotite and fluid released at sub-arc depth at different fluid/rock mass ratios (nonlinear scale; see *Materials and Methods*). The horizontal blue-shaded region in (*A*) and (*B*) indicates the minimum range of oxygen fugacity of primitive arc melts (16, 23). The oxygen fugacity of typical porphyry deposits (24) is indicated by gray-shaded field in (*A*) and (*B*). Vertical lines with double-head arrows encompass the range of fO_2 values recorded in arc magmas (24). Mineral abbreviations: Amp–amphibole, Anh–anhydrite, Bt–biotite, Chl–Chlorite, Cpx–clinopyroxene, Dol–dolomite, F–fluid, Grt–garnet, Mgs–magnesite, Ol–olivine, Opx–orthopyroxene, Pyh–pyrrhotite, Py–pyrite.

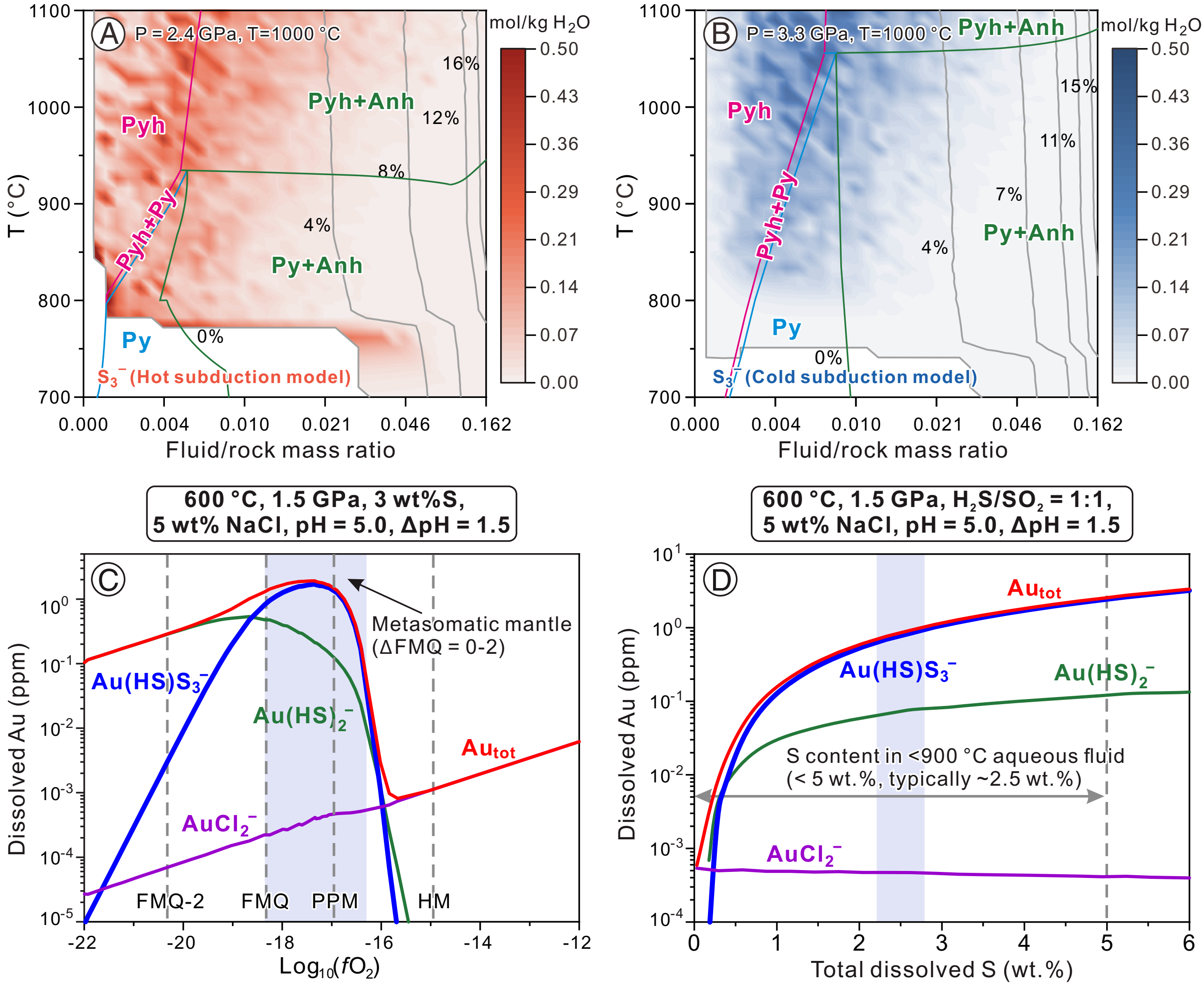

Fig. 3. Distribution of S_3^- ion and indicated gold aqueous species in slab-derived fluid upon reaction with mantle peridotite. (*A* and *B*) Orange and blue contour maps show molality of S_3^- computed for the hot and cold subduction models, respectively. Color curves outline the phase boundaries of S-bearing minerals as a function of fluid/rock ratio (nonlinear scale; see *Materials and Methods*). Gray contours state for the weight percent (wt.%) of fluid in the fluid–rock system. The color bar on the *Right* of each panel shows the concentrations of S_3^-. (*C*) Variations of gold aqueous species concentrations as a function of oxygen fugacity at pH ~ 5 as buffered by the olivine-pyroxene-garnet mantle rock assemblage at a fluid/rock mass ratio of 0.1. The vertical dashed lines show the $\log_{10}(fO_2)$ values of the FMQ, PPM, and hematite-magnetite (HM) conventional redox buffers. The oxygen fugacity of metasomatized mantle (from FMQ to ΔFMQ+2) is marked by vertical blue-shaded region (11). (*D*) The effects of total dissolved sulfur concentration on the equilibrium distribution of gold aqueous species calculated for subducted slab-derived metamorphic fluid at pH of 5 and fO_2 of the H_2S-SO_2 equilibrium (corresponding to ΔFMQ+1.5). The horizontal lines with double-head arrows and vertical blue-shaded region display the sulfur contents of aqueous fluid as constrained by experiments from ref. 25.

and sulfite (HSO_4^-, SO_4^{2-}, HSO_3^-, SO_2) persist over a wide range of temperature (*SI Appendix*, Fig. S4 *C–F*). At low fluid/rock mass ratios ($R < 0.01$), H_2S is the dominant aqueous sulfur species but the high concentrations of HS^- in the reacted aqueous fluid occur only at 800 to 900 °C, as pH changes toward more alkaline values (*SI Appendix*, Fig. S4 *A* and *B*). The highest concentrations of trisulfur radical ion S_3^- in the reacted fluid occur at 700 to 1,100 °C (Fig. 3*A*). Compared to H_2S and HS^-, S_3^- is more abundant at higher fO_2 conditions, and accounts for ≥50% of the total sulfur at fO_2 between ΔFMQ+0.5 and ΔFMQ+1.5 (Figs. 2*C* and 3*A*). At 3.3 GPa, higher concentrations of HSO_4^-, HSO_3^- and SO_2 are predicted over a wide range of temperatures and fluid/rock ratios (*SI Appendix*, Fig. S5 *C–F*). Significant concentrations of H_2S and HS^- are restricted to areas of low fluid–rock ratios and to low temperatures (<900 °C) for HS^- (*SI Appendix*, Fig. S5 *A* and *B*). At *R* values between 0.002 and 0.02 (corresponding to fO_2 from ΔFMQ–0.5 to ΔFMQ+1.5), S_3^- is the dominant aqueous sulfur species accounting for 50 to 90% of the total sulfur in the fluid (Fig. 3*B*). In both models, the abundance of S_3^- is a strong function of fO_2 and the concentrations of S_3^- are one to three orders of magnitude higher than those of HS^- at redox conditions, thus permitting sulfide-sulfate coexistence. Such concentrations are expected to favor the formation of gold complexes with the S_3^- ligand.

To support this conclusion, we calculated the speciation and solubility of gold in a metamorphic fluid (containing 3 wt.% S and 5 wt.% NaCl) typical of subduction zones at 600 °C and 1.5 GPa (Fig. 3 *C* and *D*). These calculations show that while $Au(HS)_2^-$ is the dominant gold complex below FMQ redox conditions, $Au(HS)S_3^-$ becomes the dominant gold carrier at higher oxygen fugacity, followed by $AuCl_2^-$ at highly oxidizing conditions (>ΔFMQ+3) (Fig. 3*C*). The highest abundance of $Au(HS)S_3^-$ occurs at redox conditions of the pyrite-pyrrhotite-magnetite (PPM) buffer (~ΔFMQ+1), when the gold solubility is 2 ppm (Fig. 3*C*). In addition to redox conditions, the sulfur-content of the fluid is an important parameter affecting Au solubility. At 600 °C, 1.5 GPa, and redox conditions of H_2S:SO_2=1:1, the concentration of $Au(HS)S_3^-$ complex is strongly enhanced in sulfur-rich (>1 wt.% S) fluids (Fig. 3*D*). Our calculations show that $Au(HS)S_3^-$ remains the major gold complex in sulfur-rich solutions at 700 °C and 800 °C, in which Au solubility attains 100 to 300 ppb (*SI Appendix*, Fig. S6). Gold solubility and aqueous speciation are also functions of the fluid alkalinity (here defined as $\Delta pH = pH - pH_n$, where pH_n is the pH value of the water neutrality point). At more acidic pH ($\Delta pH < -1$), $AuCl_2^-$ becomes more important, but its abundance largely decreases with increasing pH (*SI Appendix*, Fig. S7). In contrast, $Au(HS)S_3^-$ and $Au(HS)_2^-$ complexes may transport ~2 ppm Au in the aqueous fluid at neutral to alkaline conditions of ΔpH 0.0 to 2.5, which are typical of slab-derived fluids in equilibrium with mantle peridotite (*SI Appendix*, Fig. S7 and *Supplementary Text*). In summary, these mantle-wedge fluids are expected to mobilize and concentrate large amounts of Au by forming abundant $Au(HS)S_3^-$ during mantle metasomatism.

Efficiency of Gold Extraction from Oxidized Hydrous Mantle by Partial Melting. We estimated the gold extraction efficiency from a fertile mantle (containing 3.5 ppb Au and 600 ppm S) by modeling fluid-present batch melting at oxygen fugacities of ΔFMQ–1.0 (reducing) and ΔFMQ+1.5 (moderately oxidizing), respectively (Fig. 4 and *SI Appendix*, Figs. S8 and S9). Two scenarios were simulated: i) low-temperature melting (1,100 °C, 1.5 GPa) with large fractions of monosulfide solid solution (MSS) and ii) high-temperature melting (1,300 °C, 1.5 GPa) in the presence of sulfide liquid (SL). Both scenarios indicate that the consumption of mantle sulfide is favored by moderately oxidizing conditions. At fO_2 of ΔFMQ+1.5, the silicate melt contains all Au and S for a melt degree (F) of <7.5%, due to the exhaustion of sulfide (Fig. 4 *B* and *D*). At fO_2 of ΔFMQ–1.0, only a small fraction of mantle Au is released into the silicate melt at a high degree of partial melting (up to 15%, Fig. 4 *A* and *C*). Results for fluid-present melting models demonstrate that the coexistence of aqueous fluid and silicate melt is far more favorable for extraction of Au and S from mantle than in the absence of a fluid phase (Fig. 4). As shown in Fig. 4 *A* and *B*, with only 1% partial melting, ~70% of Au in the mantle can be extracted in the presence of 0.3 wt.% fluid, with concentrations of 8 ppb Au in the water-saturated melt and 800 ppb Au in the coexisting fluid. With only 5.5% melting at fO_2 of ΔFMQ+1.5 and in the presence of 0.2 wt.% fluid, mantle sulfide becomes exhausted (Fig. 4 *B* and *D*). Thus, our models reveal that the stability of sulfide liquid is greatly diminished when the fluid phase appears. This fluid phase has the ability to transport ~60 times more Au than a silicate melt at mantle-wedge conditions

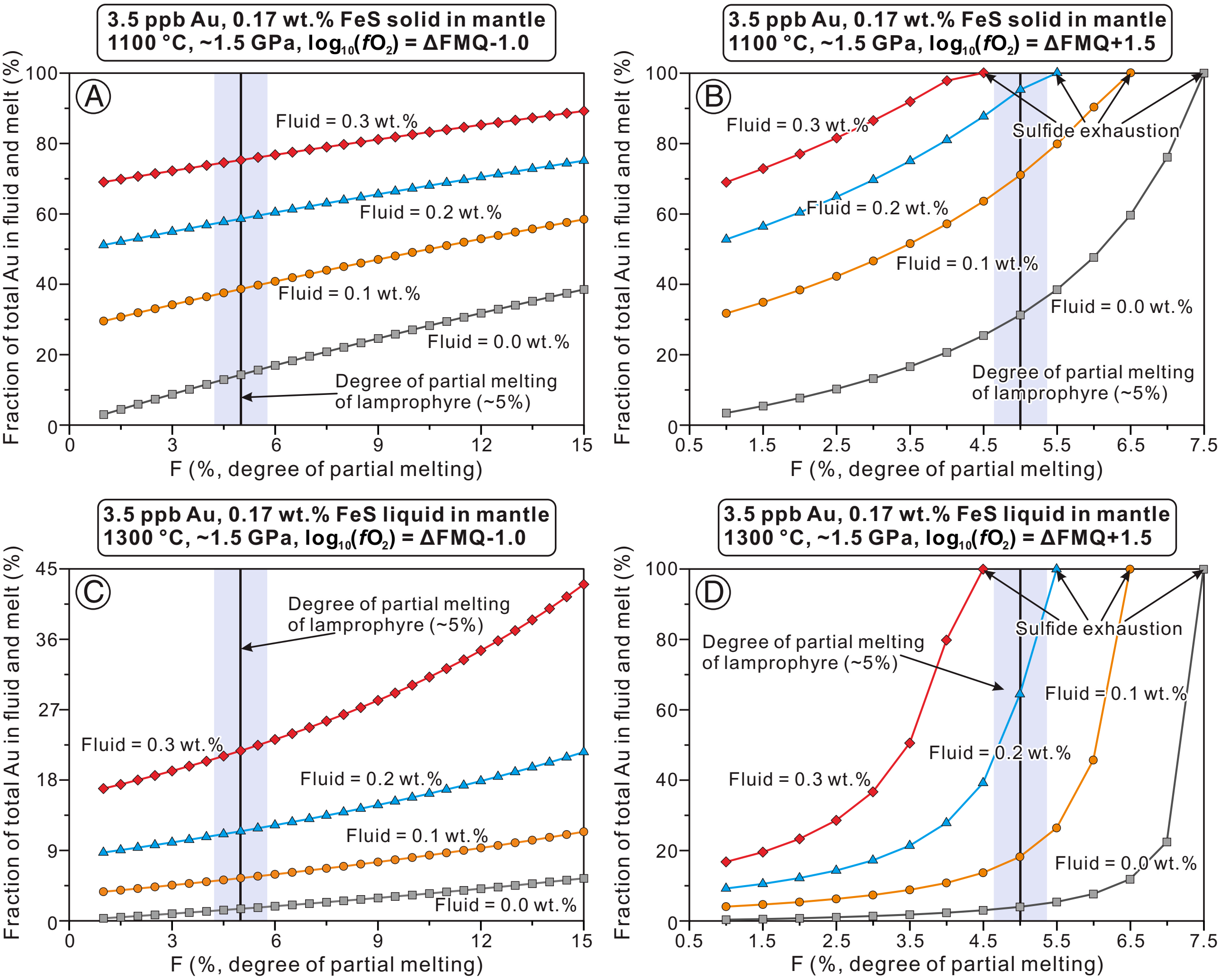

Fig. 4. Estimated total Au contents in fluid and silicate melt during hydrous mantle melting at different redox conditions. (*A* and *B*) Fractions of total Au in the fluid and melt as a function of degree of melting (F) and at different aqueous fluid contents at low-temperature melting in the stability field of MSS at redox conditions of ΔFMQ-1.0 and ΔFMQ+1.5. (*C* and *D*) Total gold fractions released into both the fluid and silicate melt (*C*) as a function of F value and for high-temperature partial melting in the presence of sulfide liquid at ΔFMQ-1.0 (*C*) and ΔFMQ+1.5 (*D*). The vertical, blue-shaded region defines a low-degree melting range, typically of 5% for lamprophyre. Fluid proportions indicated in all panels represent the assumed fraction of the free aqueous fluid of the system. The Au content released into the fluid and melt is simulated by mass balance and using experimentally available Au partition coefficients (*Materials and Methods*).

of ΔFMQ+1.5, 5% melting fraction and only 0.2 wt.% aqueous fluid in the system.

Discussion

Controls on Sulfur Mass Transfer at the Slab–Mantle Interface. Previous thermodynamic modeling (14, 26, 27) has shown that slab devolatilization releases fluids in which sulfur could be present as $CaSO_4^0$(aq), SO_4^{2-}, HSO_4^- HSO_3^-, SO_2, H_2S, and HS^-. However, these ignored the trisulfur radical ion, S_3^-, that becomes increasingly abundant at elevated temperatures and pressures. Our study reveals that S_3^- is the dominant reduced species in fluids across a wide range of redox conditions after reaction with overlying mantle (Fig. 3). Fig. 1 shows that the concentrations of sulfate and sulfite (e.g., SO_4^{2-}, HSO_4^-, HSO_3^-) in the fluid sharply increase, by one to three orders of magnitude, before reaching a plateau when pyrite is oxidized to anhydrite along both hot and cold subduction geotherms. The results presented here show that a maximum flux of oxidized fluid will be generated from AOC at 60 to 80 km and 80 to 120 km for hot and cold subduction zones, respectively. These predictions are similar to conditions at the depth of arc-magma formation. Results from the mantle infiltration model indicate that fluids released at sub-arc depth are capable of oxidizing the overlying mantle to ΔFMQ+2 to 3, whereas fluids from fore-arc depths cannot increase mantle fO_2 values to more than ΔFMQ+1 (Fig. 2). The higher oxidation state of sub-arc mantle is also consistent with the higher bulk-rock $Fe^{3+}/\Sigma Fe$ ratios of magmatic rocks (0.18 to 0.32) at volcanic arcs relative to those in back-arc, mid-ocean ridge, and fore-arc settings (6). Our predictions also fall in the fO_2 range of metasomatized mantle inferred from mantle xenoliths and arc magmas (9, 11).

As shown in Fig. 1 and *SI Appendix*, Fig. S2, increasing temperature during prograde metamorphism of the subducting slab results in the oxidation of pyrite to anhydrite and the breakdown of hydrous minerals including epidote, chlorite, and lawsonite. This process results in the growth of garnet at ~550 °C, a decrease of the $Fe^{3+}/\Sigma Fe$ ratio of clinopyroxene, and an increase of $Fe^{3+}/\Sigma Fe$ ratio in garnet with increasing temperature (*SI Appendix*, Fig. S2 *C–H*). The total Fe^{3+} content of the residual solid decreases by ~0.2 mol/kg rock over the temperature range within which pyrite is oxidized to anhydrite (*SI Appendix*, Fig. S1 *C* and *D*). From the sulfur loss curves and mineral modal abundances, ~0.03 mol/kg rock S^- (i.e., total initial sulfur content in model) is oxidized to S^{6+} when pyrite transforms to anhydrite (Fig. 1 and *SI Appendix*, Fig. S1). Consequently, mass balance calculations indicate that this redox process is consistent with the general reaction:

$$FeS_{2(solid)} + 7Fe_2O_{3(in\ silicates)} + 2CaO_{(in\ silicates\ or\ fluid)} = 2CaSO_{4(solid\ or\ in\ fluid)} + 15FeO_{(in\ silicates)}. \quad [1]$$

Our model suggests that the oxidation of S during the thermally inducted breakdown of pyrite is balanced by reduction of Fe^{3+} in bulk rock rather than reduction of CO_2 as previously proposed (14). Indeed, the bulk rock is the greatest reservoir of iron, including Fe^{3+}, which is much greater than possible CO_2 input. The results indicate that the production of sulfate in the slab is a function of the Fe^{3+} content of the protolith. It follows that the transfer of sulfate to the slab-derived fluid will leave a reduced residual mineral assemblage in the subducting oceanic crust. This conclusion is consistent with natural observations, such that the increase of core to rim $\delta^{56}Fe$ values of garnet in garnet-epidote blueschist from the Sifnos subduction zone, Greece, which was attributed to the loss of oxidizing fluids during devolatilization of the subducting slab (10). Previous thermodynamic studies concluded that the transformation of pyrite to pyrrhotite dominates the release of sulfur from the subducted slab (27). Instead, our results suggest that the oxidation of pyrite to soluble sulfate during the blueschist to eclogite transition is responsible for introducing the major fraction of oxidized sulfur from the subducted slab into the sub-arc mantle.

The mantle oxidation models presented here predict a positive correlation between the fO_2 of mantle and the increase of $Fe^{3+}/\Sigma Fe$ ratios in pyroxene and garnet with the continuous infiltration of a S^{6+}-bearing slab-derived fluid (Fig. 2 and *SI Appendix*, Fig. S3). The consumption of Fe^{2+} is manifested by an increase in the modal abundances of orthopyroxene at the expense of olivine and clinopyroxene and an increase in the X_{Mg} value of olivine (*SI Appendix*, Fig. S3 *A* and *B*). Additionally, oxidized sulfur species (HSO_4^-, SO_4^{2-}, HSO_3^-) in the infiltrating slab-derived fluid are reduced to HS^-, H_2S, and S_3^- as the fluid is reacting with the mantle rock (Fig. 3 and *SI Appendix*, Figs. S4 and S5). These sulfate reduction reactions are consistent with a decrease in fO_2 values of slab-derived fluids after interaction with depleted mantle, for instance decreasing from ΔFMQ+5 to ΔFMQ+3 at sub-arc depths (Fig. 5*A*). We therefore propose that the following schematic reactions illustrating the control of sulfur and iron redox state in the mantle wedge:

$$SO_4^{2-} + 2H^+ = H_2S + 2O_2, \quad [2]$$

$$SO_4^{2-} + 2H_2S + H^+ = S_3^- + 0.75O_2 + 2.5H_2O, \quad [3]$$

$$2FeO_{(in\ silicates)} + 0.5O_{2(in\ fluid)} = Fe_2O_{3(in\ silicates)}. \quad [4]$$

Our model predicts that fluid-altered clinopyroxene and orthopyroxene in the mantle wedge will have $Fe^{3+}/\Sigma Fe$ ratios of 0.30 to 0.45 and 0.10 to 0.20, respectively (*SI Appendix*, Fig. S3 *C* and *D*). These ratios broadly agree with analyzed values of 0.48 to 0.51 and 0.10 to 0.15 in fluid-altered metasomatic mantle peridotite from the Sulu orogeny in China (30), for clinopyroxene and orthopyroxene, respectively. Furthermore, increase of $Fe^{3+}/\Sigma Fe$ values in metasomatized garnet is consistent with values for peridotite samples of the sub-arc mantle from Bardane in Norway (13). These observations collectively indicate that the oxidized state of the mantle wedge is caused by S^{6+}-bearing slab-derived fluid metasomatism that results in the oxidation of Fe^{2+} in the silicate minerals, dissolution of sulfide minerals, and generation of reduced sulfur Au-complexing ligands such as H_2S (HS^-) and S_3^- (Fig. 5).

Enhanced Mobility and Enrichment of Gold in Mantle Wedge. Mantle wedge metasomatized by slab-derived fluids and melts generally results in enrichment in metals (e.g., up to hundreds ppb Au and thousands ppm Te) and elevated oxygen fugacity (>ΔFMQ+1) (31, 32). However, the causes of metal enrichment during mantle oxidation process were poorly understood. Recent experimental studies imply that slab melts carry no more than ¼ of the Au from the downgoing lithosphere to the overlying mantle wedge. These data are corroborated by the low gold abundances (<1 ppb) in primitive melts from subduction-related eclogite (33, 34). Although some studies have inferred Au loss into devolatilization-induced fluids by prograde sulfide breakdown during slab subduction (35, 36), this gold input cannot explain the elevated Au abundance of the overall metasomatic mantle (37). We posit an alternative model in which the mobilization and redistribution of mantle Au plays a first-order control on the formation of gold-rich metasomatized mantle by locally enhancing

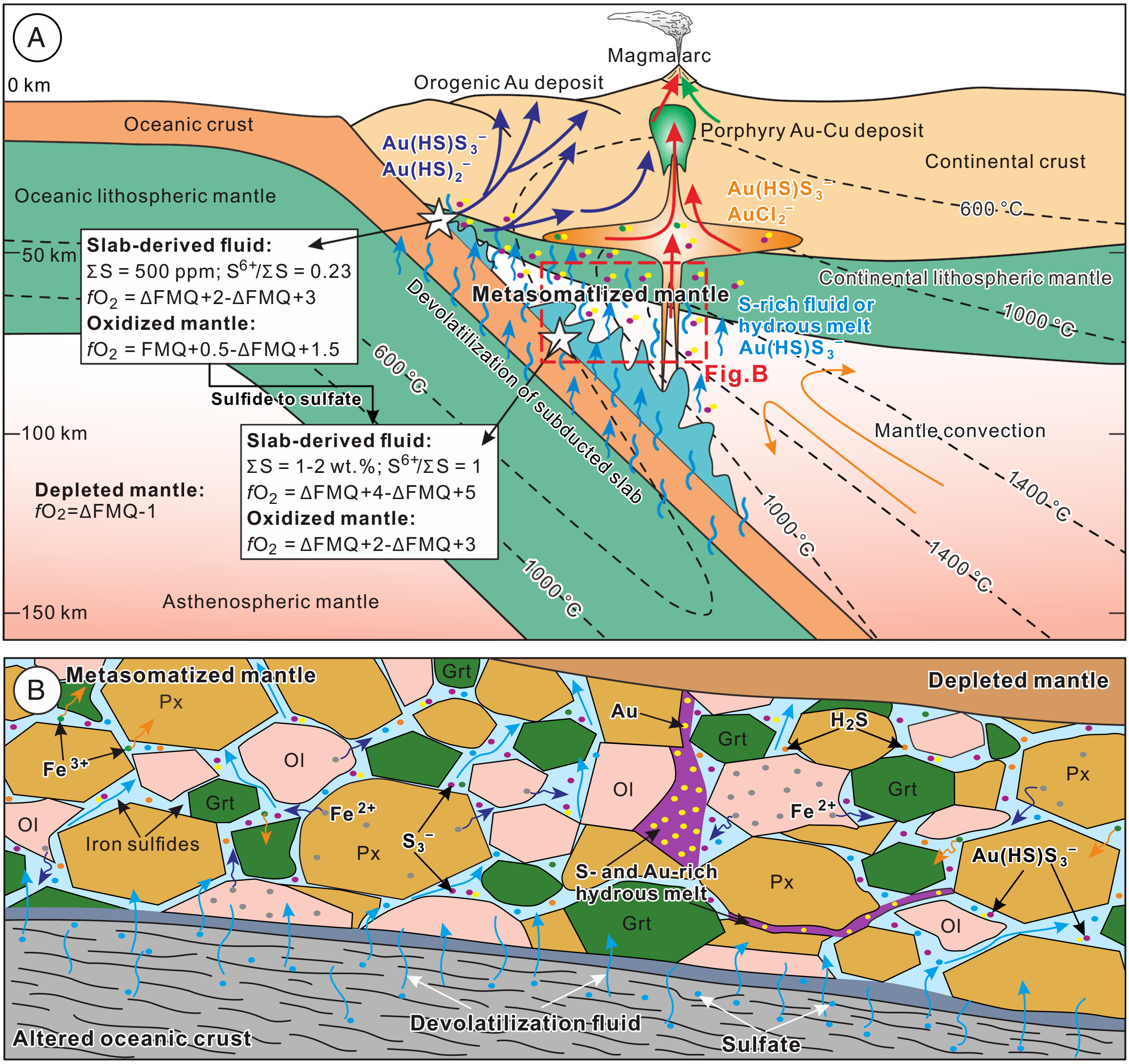

Fig. 5. Proposed scenarios for progressive devolatilization and redox processes at slab–mantle interface. (*A*) Schematic profile of a subduction zone with associated metamorphic devolatilization and magmatism (modified from refs. 28 and 29) showing the redox conditions and mobilization and concentration of sulfur and gold during mantle metasomatism as derived in this study. The white stars mark the slab depths of fore-arc and sub-arc settings. (*B*) Schematic representation of a slab-derived fluid oxidizing overlying mantle wedge and concentrating sulfur and gold. The fluid liberated from AOC carries abundant S^{6+} into the mantle wedge to oxidize Fe^{2+} in silicate minerals, thereby modifying the mantle oxidation state and leading to gold enrichment in the fluid due to reduction of S^{6+} to S_3^- and H_2S/HS^- ligands that strongly complex gold. Mineral abbreviations: Px–pyroxene; Grt–garnet; Ol–olivine.

gold fertility of mantle lithosphere. Naturalistic support for this model comes from numerous reports of gold-rich lithospheric mantle in the Ivrea Zone, Italy (31), the Deseado Massif, Argentina (38), and at Tallante, southern Spain (39). In these settings, melt- or fluid- metasomatized mantle peridotite and pyroxenite have 10 to 100 times more Au than pristine mantle and some samples even contain visible native gold particles.

A statistical analysis of mantle peridotites (40) concluded that the Au concentrations gradually increase with the evolution from deep garnet-bearing peridotite (0.5 to 1.5 ppb, max 3 ppb) to shallow plagioclase-bearing peridotite (2 to 4 ppb, max 15 ppb). The Au abundances exhibit positive correlations with the concentrations of incompatible elements in some mantle xenoliths (41). These data collectively indicate upward mobilization of Au by aqueous fluids or hydrous melts, but the abilities of fluid and melt to carry Au have not been quantified. Our numerical results show that the S-bearing fluids can carry hundreds to thousands ppb of gold as the $Au(HS)S_3^-$ complex across a wide fO_2 (FMQ to ΔFMQ+2) and pH (ΔpH = 0.0 to 2.5) due to generation of abundant S_3^- in slab-derived fluids upon reaction with depleted mantle (Fig. 3 and *SI Appendix*, Figs. S6 and S7). This enhanced transport capacity provides an explanation for the Au enrichment in oxidized metasomatic mantle (Fig. 5*B*). The consumption of these auriferous fluids during ascent through the mantle by hydration reactions would form a mantle source locally enriched in Au and volatile elements (C-O-H-S) (Fig. 5*A*). This scenario explains why sulfides hosted in weakly metasomatized mantle xenoliths (free of secondary alteration minerals) have higher gold abundances (2 ppm) in comparison to those (<0.5 ppm) hosted in strongly metasomatized rocks with secondary amphibole and apatite, such as in Spitsbergen island, Norway (42). Alternatively, the Au-rich fluids produced by subduction-modified mantle may directly contribute to the formation of gold deposits hosted in island arc zones, such as Ladolam Au deposit, Papua New Guinea (43), and volcanogenic massive sulfide gold deposit in Kermadec Arc (44). Due to a thinner lithosphere in such zones, auriferous fluid would transport abundant Au and volatiles away from residual mantle sources to domains of arc-melt generated. In summary, oxidation controls the metal enrichment in the metasomatized mantle via enhanced mobilization of Au in complex with the trisulfur radical ion in aqueous fluid under more oxidizing conditions than those of pristine mantle (Fig. 5).

Facilitated Metal Extraction and Formation of Gold Deposits. Partial melting of metasomatized mantle is regarded as a key process for the formation of porphyry Cu-Au-Mo and epithermal Au-Ag deposits (38, 45). Gold concentrations of primary mantle melts depend on the oxidation state of their source, degree of partial melting, and gold partitioning between the sulfide phases and silicate melts (18, 46, 47). Low-degree melting of oxidized mantle has been invoked to explain the formation of Au-rich parental arc magmas. For instance, ~2.4% partial melting can yield Siberian picrite that contains abnormally high concentrations of Au and platinum-group elements at redox conditions of ΔFMQ+2 (48). Furthermore, oxidized mantle xenoliths (with ΔFMQ+1 to ΔFMQ+2) from Lake Bullen Merri in Australia record extensive sulfide dissolution at very low degrees of partial melting, of ~2% (11). These data are consistent with our modeling that suggests gold is preferentially enriched in moderately oxidized (~ΔFMQ+1.5) and hydrous melts (Fig. 4 and *SI Appendix*, Figs. S8 and S9). Gold partitioning between silicate melt and sulfide is another factor influencing the Au concentration of magma. Previous experimental investigations demonstrate that iron sulfide occurs as both MSS and SL in upper mantle at redox conditions close to the sulfide-sulfate boundary (SSO, ~ΔFMQ+1.5), which is regarded as typical fO_2 conditions of metasomatized mantle (9, 49). The high Au partition coefficients (>1,000) between SL and mantle melts result in most gold being retained in the residual SL until its complete resorption at higher fO_2 (50, 51). Consequently, increasing fO_2 to higher than SSO levels by the addition of slab-derived Fe^{3+} was thought to account for the formation of Au-rich melts at high-temperature melting in the presence of sulfide liquid (18). However, our modeling quantitatively shows that the aqueous fluid only carries a few hundred ppm Fe^{3+} at sub-arc depths (*SI Appendix*, Fig. S10). Whereas slab-derived hydrous melts may carry 1 to 2 orders of magnitude more ferric iron than aqueous fluid, they are generally expected to occur at slab depths greater than 100 km (4, 18, 52). Therefore, elevating fO_2 by adding slab-derived Fe^{3+} is unlikely to be a prevalent process that promotes the release of Au from sulfide liquid. Rather, fluid-present mantle melting can scavenge gold more efficiently from mantle sulfide liquid under moderately oxidizing conditions resulting in readily exhaustion of mantle sulfides even at small degrees of partial melting (Fig. 4 and *SI Appendix*, Fig. S9). Note that the coexistence of aqueous fluid and silicate melt at our T-P conditions is consistent with experimentally established phase diagrams (53), showing fluid-melt immiscibility up to at least 3.8 GPa and 1,000 to 1,100 °C. The fluid-present partial melting of mantle wedge is also documented by the coexisting fluid and silicate melt inclusions trapped in mantle peridotite xenoliths from western Hungary (54). These findings provide a mechanism for generating Au-rich melts under redox conditions close to the coexistence of sulfide and sulfate. Our predictions are supported by natural examples such as basanitic magmas from Hawaii (formed at fO_2 of ΔFMQ+0.8) with Au concentrations up to 36 ppb (55), volatile-rich lamprophyres from Scotland, southern Africa, and the Yilgarn, Australia as the products of low-degree mantle melting having 100 to 1,000 times higher Au abundances than other "common" igneous rocks (56).

Gold grades of porphyry copper(-gold) deposits vary over three orders of magnitude, from ~0.001 to 1 ppm Au. High Au-tonnage deposits show 10 to 100 times higher average gold grades than those with high Cu tonnage (*SI Appendix*, Fig. S11). Melt inclusion data from igneous rocks that were the source of ore fluids for porphyry Cu(-Au) deposits in the Maricunga Belt, Chile, indicate that the Au concentrations of magmas were as much as three orders of magnitude higher than those reported for magmas of Cu-rich porphyry deposits (57). These differences in Au grades are likely due to the sulfur control on the deep source of metals and variation of partial melting mechanism. Our calculations suggest that the aqueous fluid acts as an extremely effective agent to transport and concentrate Au within the metasomatic mantle wedge. Mass balance calculations further indicate that 20 to 80% of the original mantle Au are released at <2% hydrous low-temperature (1,100 °C) partial melting in the stability field of MSS (Fig. 4 *A* and *B*). Therefore, the high fluid flux favors the gold enrichment into shallow mantle lithosphere by upward mobilization at active continental margins characterized by a thick lithosphere and cold mantle wedge, which, in turn leads to arc magmas derived from deep mantle becoming Au depleted. Furthermore, this enriched mantle can be stored hundreds of million years before a later tectonic melting event, as likely in the case of Lake Bullen Merri in Australia (11), and is therefore an important metal source for Au deposits formed in postsubduction settings (58). In contrast, in island arc subduction zone, high mantle temperature of >1,300 °C stabilizes the sulfide liquid, thereby resulting in >80% of the initial Au retained in mantle source rather than extracted by silicate melt until exhaustion of sulfide (Fig. 4 *C* and *D*). In these settings, according to our modeling fluid-assisted high-temperature melting of metasomatic mantle favors the generation of Au-enriched primary melts (Fig. 4 and *SI Appendix*, Fig. S9), as suggested for the high-Au arc magmas (>8 ppb) from Kermadec arc (59). Our findings thus offer another perspective for understanding the variation of Au-grade in porphyry deposits located in thick or thin lithosphere zones (60).

Previous metamorphic devolatilization scenarios explain the formation of Phanerozoic orogenic gold from a metasomatized mantle source [e.g., in Jiaodong Peninsula in China (61, 62) and in northwestern Mexico (63)]. These scenarios postulate that gold and sulfur are released into the fluids through breakdown of pyrite to pyrrhotite, conditions at which H_2S and HS^- are postulated to be the ligands transporting gold (64). In contrast, our numerical modeling reveals that the sulfide-sulfate transition provides the most favorable window for sulfur release under conditions typical of the metasomatized mantle. At such conditions, the high abundance of S_3^- enables at least 10 to 100 times more efficient mobilization of gold by S-rich fluids than any common ligand such as H_2S, HS^- or Cl^- (Fig. 3 *C* and *D*). The breakdown of S_3^- at lower temperatures and pressures would trigger efficient and focused Au precipitation in upper levels of the crust where most deposits form (20, 65). Consequently, S_3^- may be a key factor ensuring the generation of an auriferous fluid in metasomatized mantle lithosphere (Fig. 5). In conclusion, our results demonstrate that mantle oxidation by S-bearing aqueous fluids is the key trigger mechanism for Au enrichment and release within mantle wedge, providing both the necessary source and transport conditions for the formation of gold-rich porphyry-epithermal and orogenic gold systems. Additional works on both chemical and physical reactive transport models will be a priority to advance our understanding of metal enrichment and the transfer of the fluid-saturated silicate melt through the mantle wedge and its ascent to shallower crust levels in subduction zones.

Materials and Methods

System Compositions and Redox Budgets (RBs). Bulk rock compositions chosen to model the altered oceanic crust and depleted mantle peridotite systems were modified from refs. 66 and 67 (*SI Appendix*, Tables S1 and S2). Different water contents were chosen for the hot and cold subduction zone regimes to enable H_2O saturation at the first P-T point, with contents of 4.7 and 7.6 wt.%, respectively. The RB is a critical variable for quantifying the potential redox capacity of a rock-fluid system, which is defined as

$$\mathrm{RB} = \sum n_j v_j,$$

where v_j represents the number of electrons per mole required to convert a redox-sensitive element from a reduced state to the reference oxidation state, and n_j is the number of moles of the element per 1 kg of fluid–rock system. Here, we only define the RB of initial solid rock, as the remainder can be calculated using the thermodynamic modeling software. Iron, carbon, and sulfur were considered to be the major redox-sensitive elements in our model. For depleted mantle peridotite, the initial oxidation states of iron, carbon, and sulfur were set as Fe^{2+}, C^0, and S^{2-}, with minor Fe^{3+} corresponding to an $Fe^{3+}/\Sigma Fe$ ratio of 0.031 (15). In view of the limited contents of CO_2 (50 ppm) in the depleted mantle, their influence on the model results is negligible. Compared with the juvenile oceanic crust, the altered oceanic crust is characterized by higher $Fe^{3+}/\Sigma Fe$ values, which were adopted as 0.51. The redox states of sulfur were adopted to be S^- in pyrite and S^{6+} in anhydrite with concentrations of 700 ppm and 364 ppm S, respectively. The composition of the modeled rocks is listed in *SI Appendix*, Table S1.

Phase Equilibrium Modeling. Our modeling includes a devolatilization model of AOC along hot and cold subduction paths, and a mantle infiltration model. The geothermal models of Central Honshu and Central Cascadia subduction zones were chosen to represent, respectively, the cold and hot thermal regime of the subducting slab (22). The devolatilization model was calculated along the top-of-slab P-T paths in both geothermal regimes, and each geotherm was discretized into 671 P-T points from 0.50 GPa to 7.20 GPa with a step of 0.01 GPa. When simulating the devolatilization processes of the subducting slab, the fluid produced at a given P-T point was separated from the bulk rock. To quantify the relative oxidation capacity of the slab-derived fluid, two methods were employed in simulating mantle infiltration processes: a titration scenario and a mixing scenario. In the former, fluid compositions were extracted from three different slab depths (Fig. 1), then equilibrated with model mantle peridotite at 3.3 GPa, 1,000 °C, and 2.4 GPa, 1,000 °C for cold and hot subduction models, respectively. The extracted fluid composition was normalized to 2 moles of hydrogen (H), which is roughly equivalent to 1 mol of H_2O-dominated fluid, corresponding to 18 g (*SI Appendix*, Table S3). We divided 12 moles of such a fluid into 120 equal portions of 0.1 mole, and added one portion into 1 kg of model peridotite at each subsequent step. In the mixing scenario, 1 mol of fluid (normalized to 2 moles of H) released at sub-arc depth as an endmember was reacted with 1 kg of mantle peridotite as the other endmember at different fluid/rock mass ratios, from 700 °C to 1,100 °C. The compositions of 1 mol fluid and 1 kg rock are expressed here as elemental concentrations in numbers of moles (*SI Appendix*, Tables S2 and S3). The fluid–rock ratio increases nonlinearly due to the following dependence between the masses of reacting fluid and rock in a mixing model:

$$\mathrm{R} = \frac{\mathrm{m}_{fluid} \times \mathrm{X}_{fluid}}{\mathrm{m}_{rock} \times (1 - \mathrm{X}_{fluid})},$$

where R is fluid–rock mass ratio of the system at a specific X_{fluid} value, and m_{fluid} and m_{rock} represent initial masses of fluid (18 g) and mantle peridotite (1,000 g), respectively. The X_{fluid} is an independent variable with values between 0 and 1. For example, an X_{fluid} value of 0.9 on this scale corresponds to a mass fluid/rock ratio of 0.16. All calculations were executed by Gibbs energy minimization in Perple_X 7.0.11 (14, 68), using so called "lagged speciation" method of Perple_X to compute the concentrations of aqueous species (14). Both for the devolatilization and mantle oxidation models, the fluid was considered as a H_2O-CO_2 binary solution (14). Thermodynamic data for aqueous species (except S_3^-) are taken from the SUCRT92 database (69) complemented by the Deep Earth Water (DEW) model for Ca, Mg, Fe, Al, and Si species (70) and those for minerals from the revised Holland and Powell mineral database (71). The thermodynamic parameters of S_3^- are taken from ref. 65 based on direct experimental measurements and revised Helgeson-Kirkham-Flowers (HKF) equation of state compatible with the DEW model. Organic species were excluded from the calculations. Amphibole, biotite, chlorite, clinopyroxene, dolomite, epidote, feldspar, garnet, magnesite, muscovite, pumpellyite, pyrrhotite, olivine, orthopyroxene, stilpnomelane, and talc were treated as solid solutions. All other minerals were treated as pure phase compounds, including albite, anhydrite, coesite, kyanite, lawsonite, pyrite, quartz, and stilbite. For more details on solid solution models and fluid equations of state see *SI Appendix*, Tables S4 and S5.

Modeling of Au Speciation and Solubility in the Fluid Phase. Gold speciation and solubility in H_2O-NaCl-S aqueous fluids at 1.5 GPa, 600 °C, which are typical dehydration conditions of AOC and serpentinized oceanic mantle, were modeled to explore the geochemical behavior of Au during mantle metasomatism. The main fluid constituents include 6 wt.% NaCl (72), 3 wt.% S (25), and an excess of native gold. The fluid pH was buffered at a value of about 5 by using the olivine-pyroxene-garnet mantle mineral assemblage, which corresponds to slightly alkaline conditions relative to the neutrality point of pure water ($\Delta pH = 1.5$ to 2.5; see *SI Appendix*). The thermodynamic properties of minerals and major fluid constituents, including most sulfur species, are from the updated Holland and Powell (73) and SUPCRT databases (69), respectively. The HKF equation of state parameters for the S_3^- ion were adopted from ref. 65. The complexes $Au(HS)_2^-$, $AuCl_2^-$, and $Au(HS)S_3^-$, for which robust thermodynamic data were constrained over a wide P-T range (20, 74, 75), were considered in the modeling. Species such as $AuHS^0$, $AuHS(H_2S)_3{}^0$, $AuOH^0$, $AuCl^0$, and $Au(OH)_2^-$ were ignored because of the large uncertainties associated with their identity and stability at elevated temperatures and inconsistencies in their published thermodynamic parameters. Sources of the thermodynamic properties of Au-HS-Cl-S_3^- species are reported in *SI Appendix*, Table S5. These datasets arise from the large amount of experimental work described by the HKF equation of state, which enables plausible extrapolations to the high temperatures and pressures of our system. Calculations were conducted using the HCh package and modified and updated Unitherm database (76).

Estimation of Gold Extraction during Hydrous Mantle Melting. The available partial melting models disregard the effects of an aqueous fluid phase on the element distribution. In this study, we applied mass balance relationships to quantify the Au contents released into the fluid and silicate melt during partial melting of mantle. We calculated a batch melting process at a given free aqueous fluid phase fraction varying from 0.1 to 0.3 wt.% of the melt-fluid-rock system. Mantle Au is stored almost exclusively by iron sulfide solid or liquid with negligible Au fractions in other silicate minerals or as a metallic gold particle. Therefore, the total Au content in a closed system at equilibrium is given by the following equation:

$$M_{Au} = C_{Au}^{sul} \times M_{sulfide} + C_{Au}^{fluid} \times m_{fluid} \times C_{Au}^{melt} \times m_{melt},$$

where M_{Au} is the total *Au* content per unit mass of mantle rock, $m_{(j)}$ and $C_{Au}^{(j)}$ are the mass fraction and Au concentrations of the iron sulfide phase, aqueous fluid phase, and silicate melt phase, respectively. According to the gold partition coefficients of sulfide/melt ($D_{Au}^{sulide/melt}$) and fluid/melt ($D_{Au}^{fluid/melt}$), the above equation can be re-arranged to express the Au concentration in silicate melt:

$$C_{Au}^{melt} = \frac{M_{Au}}{D_{Au}^{sulfide/melt} \times m_{sulfide} + D_{Au}^{fluid/melt} \times m_{fluid} + m_{melt}}.$$

The Au concentrations in aqueous fluid and sulfide can thus be estimated by mass balance in close-system batch melting, which is given by

$$C_{Au}^{fluid} = C_{Au}^{melt} \times D_{Au}^{fluid/melt}; C_{Au}^{sulfide} = C_{Au}^{melt} \times D_{Au}^{sulide/melt}.$$

The mass fraction of melt, m_{melt}, depends on the melting degree, *F*, the mass fraction of residual sulfur in mantle rock at any given *F* value, and the fluid content:

$$M_S^{rock} = M_{St}^{i} - C_S^{fluid} \times m_{fluid} - C_s^{melt} \times F,$$

where M_S^{rock} and $M_{S_t}^{i}$ represent the residual and initial sulfur content in mantle rock, C_S^{fluid} and C_S^{melt} are sulfur concentrations that solubilities in aqueous fluid and mantle melts, which were determined by regression of the available experimental data (*SI Appendix*, Fig. S12). Sulfide has long been known to occur as both MSS and SL phases at upper mantle temperature and pressure, and its phase state (solid or liquid) exerts a first-order control on Au partitioning during mantle melting (48, 51). Available experimental data indicate that MSS and SL are stable, respectively, at <1,200 °C and ≥1,300 °C, at pressures of 1.5 GPa, corresponding to mantle partial melting depths (49). Therefore, in our melting model, two scenarios, a high-temperature (1,300 °C) and a low-temperature (1,100 °C) one, for hydrous mantle melting were simulated at two different redox conditions, of ΔFMQ+1.5 and ΔFMQ−1.0. The initial Au concentration of metasomatized mantle was assumed to be 3.5 ppb (40), and the sulfur concentration was chosen to be 600 ppm, corresponding to 0.17 wt.% of MSS in the system (77). The partition coefficients of Au between MSS or SL, and aqueous fluid and silicate melts are from the available experimental data (50, 78) whose typical values for the conditions of our study were adopted as $D_{Au}^{MSS/melt}$ of 200, $D_{Au}^{SL/melt}$ of 2200, and $D_{Au}^{fluid/melt}$ of 100. These data, both on sulfur solubility and Au partitioning are from direct fluid-saturated melting experiments, thereby allowing gold extraction from metasomatic mantle via hydrous melting to be estimated (see *SI Appendix* for more details for model limitations and uncertainties).

Data, Materials, and Software Availability. All study data are included in the article and/or *SI Appendix*.

ACKNOWLEDGMENTS. K.-F.Q. and J.D. acknowledge Professor Richard Goldfarb and David Groves for their insights and discussions on the theme of gold enrichment within metasomatic mantle throughout the years. K.-F.Q. thanks the position of guest professor granted by Université de Toulouse III Paul Sabatier. This work was supported by the High-performance Computing Platform of China University of Geosciences Beijing. This research was financially supported by the National Natural Science Foundation of China (42130801, 42261134535, and 42072087), the National Key Research Program (2023YFF0804200 and 2023YFC2906900), the Frontiers Science Center for Deep-time Digital Earth (2652023001), and the 111 Project of the Ministry of Science and Technology (BP0719021), Shandong Provincial Bureau of Geology and Mineral Resources No.6 Geological Brigade (LDKJ20240101). A.C.S. acknowledges funding from the U.S. NSF Earth Sciences Grants 2214119 and 2233425. G.S.P. acknowledges funding from the Institut Carnot ISIFoR (grant AsCOCrit) and the CNRS through the Mission pour les initiatives transverses et interdisciplinaires interdisciplinary program "Conditions Extremes 2024" (grant ExtremeS). Last, we are grateful to Editors May R. Berenbaum, Huda Akil, and T.P. and two anonymous reviewers whose constructive comments greatly improved the article.

Author affiliations: [a]Frontiers Science Center for Deep-time Digital Earth, State Key Laboratory of Geological Processes and Mineral Resources, School of Earth Sciences and Resources, China University of Geosciences, Beijing 100083, China; [b]Experimental Geosciences Team, Géosciences Environnement Toulouse, Observatoire Midi-Pyrénées, CNRS, Institut de Recherche pour le Développement, Université de Toulouse III Paul Sabatier, Toulouse F-31400, France; [c]Department of Earth and Environmental Sciences, University of Michigan, Ann Arbor, MI 48109; [d]Department of Earth Sciences, ETH Zurich, Zürich 8092, Switzerland; [e]School of Science, China University of Geosciences, Beijing 100083, China; [f]Department of Earth and Environmental Sciences, Macquarie University, Sydney, NSW 2109, Australia; and [g]Geological Research Institute of Shandong Gold Group Co., Ltd., Jinan 250013, China

1. J. J. Ague *et al.*, Slab-derived devolatilization fluids oxidized by subducted metasedimentary rocks. *Nat. Geosci.* **15**, 320–326 (2022).
2. T. Kawamoto *et al.*, Mantle wedge infiltrated with saline fluids from dehydration and decarbonation of subducting slab. *Proc. Natl. Acad. Sci. U.S.A.* **110**, 9663–9668 (2013).
3. W. Sun, R. J. Arculus, V. S. Kamenetsky, R. A. Binns, Release of gold-bearing fluids in convergent margin magmas prompted by magnetite crystallization. *Nature* **431**, 975–978 (2004).
4. K. Mibe, T. Kawamoto, K. N. Matsukage, Y. Fei, S. Ono, Slab melting versus slab dehydration in subduction-zone magmatism. *Proc. Natl. Acad. Sci. U.S.A.* **108**, 8177–8182 (2011).
5. T. Plank, C. E. Manning, Subducting carbon. *Nature* **574**, 343–352 (2019).
6. K. A. Kelley, E. Cottrell, Water and the oxidation state of subduction zone magmas. *Science* **325**, 605–607 (2009).
7. J. C. M. D. Hoog, E. Clarke, K. Hattori, Mantle wedge olivine modifies slab-derived fluids: Implications for fluid transport from slab to arc magma source. *Geology* **51**, 663–667 (2023).
8. P. Tollan, J. Hermann, Arc magmas oxidized by water dissociation and hydrogen incorporation in orthopyroxene. *Nat. Geosci.* **12**, 667–671 (2019).
9. A. Bénard *et al.*, Oxidising agents in sub-arc mantle melts link slab devolatilisation and arc magmas. *Nat. Commun.* **9**, 3500 (2018).
10. A. R. Gerrits *et al.*, Release of oxidizing fluids in subduction zones recorded by iron isotope zonation in garnet. *Nat. Geosci.* **12**, 1029–1033 (2019).
11. A. Rielli *et al.*, Incipient metal and sulfur extraction during melting of metasomatised mantle. *Earth Planet. Sci. Lett.* **599**, 117850 (2022).
12. M. J. Muth, P. J. Wallace, Slab-derived sulfate generates oxidized basaltic magmas in the southern Cascade arc (California, USA). *Geology* **49**, 1177–1181 (2021).
13. A. Rielli *et al.*, Evidence of sub-arc mantle oxidation by sulphur and carbon. *Geochem. Persp. Lett.* **3**, 124–132 (2017).
14. J. A. D. Connolly, M. E. Galvez, Electrolytic fluid speciation by Gibbs energy minimization and implications for subduction zone mass transfer. *Earth Planet. Sci. Lett.* **501**, 90–102 (2018).
15. J. A. Padrón-Navarta, V. López Sánchez-Vizcaíno, M. D. Menzel, M. T. Gómez-Pugnaire, C. J. Garrido, Mantle wedge oxidation from deserpentinization modulated by sediment-derived fluids. *Nat. Geosci.* **16**, 268–275 (2023).
16. M. J. Muth, P. J. Wallace, Sulfur recycling in subduction zones and the oxygen fugacity of mafic arc magmas. *Earth Planet. Sci. Lett.* **599**, 117836 (2022).
17. Z. Taracsák *et al.*, Sulfur from the subducted slab dominates the sulfur budget of the mantle wedge under volcanic arcs. *Earth Planet. Sci. Lett.* **602**, 117948 (2023).
18. J. E. Mungall, Roasting the mantle: Slab melting and the genesis of major Au and Au-rich Cu deposits. *Geology* **30**, 915–918 (2002).
19. R. E. Botcharnikov *et al.*, High gold concentrations in sulphide-bearing magma under oxidizing conditions. *Nat. Geosci.* **4**, 112–115 (2011).
20. G. S. Pokrovski, N. N. Akinfiev, A. Y. Borisova, A. V. Zotov, K. Kouzmanov, Gold speciation and transport in geological fluids: Insights from experiments and physical-chemical modelling. *Geol. Soc. Lond. Spec. Publ.* **402**, 9–70 (2014).
21. G. S. Pokrovski, L. S. Dubrovinsky, The S_3^- ion is stable in geological fluids at elevated temperatures and pressures. *Science* **331**, 1052–1054 (2011).
22. E. M. Syracuse, P. E. van Keken, G. A. Abers, The global range of subduction zone thermal models. *Phys. Earth Planet. Inter.* **183**, 73–90 (2010).
23. D. H. Green, W. O. Hibberson, I. Kovács, A. Rosenthal, Water and its influence on the lithosphere–asthenosphere boundary. *Nature* **467**, 448–451 (2010).
24. K. Hattori, Porphyry copper potential in Japan based on magmatic oxidation state. *Resour. Geol.* **68**, 126–137 (2018).
25. S. Jégo, R. Dasgupta, Fluid-present melting of sulfide-bearing ocean-crust: Experimental constraints on the transport of sulfur from subducting slab to mantle wedge. *Geochim. Cosmochim. Acta* **110**, 106–134 (2013).
26. J. B. Walters, A. M. Cruz-Uribe, H. R. Marschall, Sulfur loss from subducted altered oceanic crust and implications for mantle oxidation. *Geochem. Persp. Lett.* **13**, 36–41 (2020).
27. A. G. Tomkins, K. A. Evans, Separate zones of sulfate and sulfide release from subducted mafic oceanic crust. *Earth Planet. Sci. Lett.* **428**, 73–83 (2015).
28. D. A. Holwell *et al.*, Mobilisation of deep crustal sulfide melts as a first order control on upper lithospheric metallogeny. *Nat. Commun.* **13**, 573 (2022).
29. J. J. Wilkinson, Triggers for the formation of porphyry ore deposits in magmatic arcs. *Nat. Geosci.* **6**, 917–925 (2013).
30. N. Malaspina, F. Langenhorst, P. Fumagalli, S. Tumiati, S. Poli, Fe^{3+} distribution between garnet and pyroxenes in mantle wedge carbonate-bearing garnet peridotites (Sulu, China) and implications for their oxidation state. *Lithos* **146–147**, 11–17 (2012).
31. D. A. Holwell *et al.*, A metasomatized lithospheric mantle control on the metallogenic signature of post-subduction magmatism. *Nat. Commun.* **10**, 3511 (2019).
32. K.-F. Qiu *et al.*, The role of an oxidized lithospheric mantle in gold mobilization. *Sci. Adv.* **10**, eado6262 (2024).
33. Z. Zou *et al.*, Deep mantle cycle of chalcophile metals and sulfur in subducted oceanic crust. *Geochim. Cosmochim. Acta* **370**, 15–28 (2024).
34. Y. Li *et al.*, An essential role for sulfur in sulfide-silicate melt partitioning of gold and magmatic gold transport at subduction settings. *Earth Planet. Sci. Lett.* **528**, 115850 (2019).
35. S. Aulbach *et al.*, Siderophile and chalcophile elements in spinels, sulphides and native Ni in strongly metasomatised xenoliths from the Bultfontein kimberlite (South Africa). *Lithos* **380–381**, 105880 (2021).
36. J. B. Walters, A. M. Cruz-Uribe, H. R. Marschall, B. Boucher, The role of sulfides in the chalcophile and siderophile element budget of the subducted oceanic crust. *Geochim. Cosmochim. Acta* **304**, 191–215 (2021).
37. Z. Wang *et al.*, Metasomatized lithospheric mantle for Mesozoic giant gold deposits in the North China craton. *Geology* **48**, 169–173 (2019).
38. S. Tassara *et al.*, Plume-subduction interaction forms large auriferous provinces. *Nat. Commun.* **8**, 843 (2017).
39. J. M. González-Jiménez *et al.*, Mineralogy of the HSE in the subcontinental lithospheric mantle—An interpretive review. *Lithos* **372–373**, 105681 (2020).
40. J. E. Saunders, N. J. Pearson, S. Y. O'Reilly, W. L. Griffin, Gold in the mantle: A global assessment of abundance and redistribution processes. *Lithos* **322**, 376–391 (2018).
41. P. Kepezhinskas, M. J. Defant, E. Widom, Abundance and distribution of PGE and Au in the island-arc mantle: Implications for sub-arc metasomatism. *Lithos* **60**, 113–128 (2002).
42. J. E. Saunders, N. J. Pearson, S. Y. O'Reilly, W. L. Griffin, Sulfide metasomatism and the mobility of gold in the lithospheric mantle. *Chem. Geol.* **410**, 149–161 (2015).
43. B. I. A. McInnes, J. S. McBride, N. J. Evans, D. D. Lambert, A. S. Andrew, Osmium isotope constraints on ore metal recycling in subduction zones. *Science* **286**, 512–516 (1999).
44. C. Timm, C. E. J. de Ronde, M. I. Leybourne, D. Layton-Matthews, I. J. Graham, Sources of chalcophile and siderophile elements in Kermadec arc lavas. *Econ. Geol.* **107**, 1527–1538 (2012).
45. A. C. Simon, E. M. Ripley, The role of magmatic sulfur in the formation of ore deposits. *Rev. Mineral. Geochem.* **73**, 513–578 (2011).
46. J. P. Richards, Giant ore deposits formed by optimal alignments and combinations of geological processes. *Nat. Geosci.* **6**, 911–916 (2013).
47. J. E. Mungall, J. J. Hanley, N. T. Arndt, A. Debecdelievre, Evidence from meimechites and other low-degree mantle melts for redox controls on mantle-crust fractionation of platinum-group elements. *Proc. Natl. Acad. Sci. U.S.A.* **103**, 12695–12700 (2006).

48. J. E. Mungall, D. R. A. Andrews, L. J. Cabri, P. J. Sylvester, M. Tubrett, Partitioning of Cu, Ni, Au, and platinum-group elements between monosulfide solid solution and sulfide melt under controlled oxygen and sulfur fugacities. *Geochim. Cosmochim. Acta* **69**, 4349–4360 (2005).
49. Z. Zhang, M. M. Hirschmann, Experimental constraints on mantle sulfide melting up to 8 GPa. *Am. Mineral.* **101**, 181–192 (2016).
50. R. E. Botcharnikov *et al.*, Behavior of gold in a magma at sulfide-sulfate transition: Revisited. *Am. Mineral.* **98**, 1459–1464 (2013).
51. J. E. Mungall, J. M. Brenan, Partitioning of platinum-group elements and Au between sulfide liquid and basalt and the origins of mantle-crust fractionation of the chalcophile elements. *Geochim. Cosmochim. Acta* **125**, 265–289 (2014).
52. C. Tiraboschi *et al.*, Preferential mobilisation of oxidised iron by slab-derived hydrous silicate melts. *Geochem. Persp. Lett.* **24**, 43–47 (2023).
53. K. Mibe *et al.*, Second critical endpoint in the peridotite-H_2O system. *J. Geophys. Res.: Solid Earth* **112**, B03201 (2007).
54. K. Hidas *et al.*, Coexisting silicate melt inclusions and H2O-bearing, CO2-rich fluid inclusions in mantle peridotite xenoliths from the Carpathian-Pannonian region (central Hungary). *Chem. Geol.* **274**, 1–18 (2010).
55. T. W. Sisson, Native gold in a Hawaiian alkalic magma. *Econ. Geol.* **98**, 643–648 (2003).
56. N. M. S. Rock, D. I. Groves, Do lamprophyres carry gold as well as diamonds? *Nature* **332**, 253–255 (1988).
57. J. T. Ovalle, A. C. Simon, M. Schirra, Z. Zajacz, "Understanding the genesis of gold-rich porphyry systems: A case of study from the dorado porphyry gold deposit in the Maricunga Belt, Northern Chile" in *AGU Fall Meeting Abstracts* (Chicago, IL, 2022), pp. V43A-04.
58. J. P. Richards, Postsubduction porphyry Cu-Au and epithermal Au deposits: Products of remelting of subduction-modified lithosphere. *Geology* **37**, 247–250 (2009).
59. C. Timm *et al.*, Hydrous mantle melting controls gold enrichment in Kermadec arc magmas. Research Square [Preprint] (2024). https://doi.org/10.21203/rs.3.rs-4680224/v1 (Accessed 7 June 2024).
60. J.-W. Park, I. H. Campbell, M. Chiaradia, H. Hao, C.-T. Lee, Crustal magmatic controls on the formation of porphyry copper deposits. *Nat. Rev. Earth Environ.* **2**, 542–557 (2021).
61. K. F. Qiu *et al.*, Gold deposits of the Jiaodong Peninsula, eastern China. *SEG Spec. Publ.* **23**, 753–773 (2020).
62. J. Deng *et al.*, An integrated mineral system model for the gold deposits of the giant Jiaodong province, eastern China. *Earth Sci. Rev.* **208**, 103274 (2020).
63. A. Izaguirre *et al.*, Tectonic framework for Late Cretaceous to Eocene quartz-gold vein mineralization from the Caborca Orogenic Gold Belt in Northwestern Mexico. *Econ. Geol.* **112**, 1509–1529 (2017).
64. D. I. Groves, L. Zhang, M. Santosh, Subduction, mantle metasomatism, and gold: A dynamic and genetic conjunction. *GSA Bulletin* **132**, 1419–1426 (2019).
65. G. S. Pokrovski, J. Dubessy, Stability and abundance of the trisulfur radical ion S_3^- in hydrothermal fluids. *Earth Planet. Sci. Lett.* **411**, 298–309 (2015).
66. K. A. Kelley, T. Plank, J. Ludden, H. Staudigel, Composition of altered oceanic crust at ODP Sites 801 and 1149. *Geochem. Geophys. Geosyst.* **4**, 8910 (2003).
67. V. J. M. Salters, A. Stracke, Composition of the depleted mantle. *Geochem. Geophys. Geosyst.* **5**, Q05B07 (2004).
68. M. E. Galvez, J. A. D. Connolly, C. E. Manning, Implications for metal and volatile cycles from the pH of subduction zone fluids. *Nature* **539**, 420–424 (2016).
69. J. W. Johnson, E. H. Oelkers, H. C. Helgeson, SUPCRT92: A software package for calculating the standard molal thermodynamic properties of minerals, gases, aqueous species, and reactions from 1 to 5000 bar and 0 to 1000 °C. *Comput. Geosci.* **18**, 899–947 (1992).
70. F. Huang, D. A. Sverjensky, Extended deep earth water model for predicting major element mantle metasomatism. *Geochim. Cosmochim. Acta* **254**, 192–230 (2019).
71. T. J. B. Holland, R. Powell, An improved and extended internally consistent thermodynamic dataset for phases of petrological interest, involving a new equation of state for solids. *J. Metamorph. Geol.* **29**, 333–383 (2011).
72. Y. Huang, T. Nakatani, M. Nakamura, C. McCammon, Saline aqueous fluid circulation in mantle wedge inferred from olivine wetting properties. *Nat. Commun.* **10**, 5557 (2019).
73. T. Holland, R. Powell, An improved and extended internally consistent thermodynamic dataset for phases of petrological interest, involving a new equation of state for solids. *J. Metamorph. Geol.* **29**, 333–383 (2011).
74. G. S. Pokrovski *et al.*, Sulfur radical species form gold deposits on Earth. *Proc. Natl. Acad. Sci. U.S.A.* **112**, 13484–13489 (2015).
75. K. Rauchenstein-Martinek, T. Wagner, M. Wälle, C. A. Heinrich, Gold concentrations in metamorphic fluids: A LA-ICPMS study of fluid inclusions from the Alpine orogenic belt. *Chem. Geol.* **385**, 70–83 (2014).
76. Y. V. Shvarov, HCh: New potentialities for the thermodynamic simulation of geochemical systems offered by windows. *Geochem. Int.* **46**, 834–839 (2008).
77. J. C. M. de Hoog, P. R. D. Mason, M. J. van Bergen, Sulfur and chalcophile elements in subduction zones: Constraints from a laser ablation ICP-MS study of melt inclusions from Galunggung Volcano, Indonesia. *Geochim. Cosmochim. Acta* **65**, 3147–3164 (2001).
78. Z. Zajacz, P. A. Candela, P. M. Piccoli, M. Wälle, C. Sanchez-Valle, Gold and copper in volatile saturated mafic to intermediate magmas: Solubilities, partitioning, and implications for ore deposit formation. *Geochim. Cosmochim. Acta* **91**, 140–159 (2012).

PNAS

Supporting Information for

Mantle oxidation by sulfur drives the formation of giant gold deposits in subduction zones

Deng-Yang He[1], Kun-Feng Qiu[1, 2*], Adam C. Simon[3], Gleb S. Pokrovski[2], Hao-Cheng Yu[1], James A. D. Connolly[4], Shan-Shan Li[5], Simon Turner[6], Qing-Fei Wang[1], Meng-Fan Yang[1], Jun Deng[1, 7*]

[1] Frontiers Science Center for Deep-time Digital Earth, State Key Laboratory of Geological Processes and Mineral Resources, School of Earth Sciences and Resources, China University of Geosciences, Beijing, 100083, China

[2] Experimental Geosciences Team, Géosciences Environnement Toulouse (GET), Observatoire Midi-Pyrénées, Université de Toulouse III Paul Sabatier, Centre National de la Recherche Scientifique (CNRS), Institut de Recherche pour le Développement (IRD), 14, avenue Edouard Belin, F-31400 Toulouse, France

[3] Department of Earth and Environmental Sciences, University of Michigan, Ann Arbor, MI, USA

[4] Department of Earth Sciences, ETH Zurich, Zürich, Switzerland

[5] School of Science, China University of Geosciences, Beijing 100083, China

[6] Department of Earth and Environmental Sciences, Macquarie University, Sydney 2109, Australia

[7] Geological Research Institute of Shandong Gold Group Co., Ltd., Jinan 250013, China

* Kun-Feng Qiu, Jun Deng

Email: kunfengqiu@qq.com, djun@cugb.edu.cn

This PDF file includes:

- Supporting text
- Figures S1 to S12
- Tables S1 to S6
- SI References

Supporting Information Text

Oxygen fugacity calculation in Perple_X

The fO_2 values in the fluid-mineral systems of this study are calculated by converting the chemical potential of O_2 using the following equation:

$$fO_2 = e^{([\mu O_2{}^{T,P} - G^0 O_{2,\text{pure gas}}{}^{T,1\text{bar}}]/[RT])}$$

where $\mu O_2{}^{T,P}$ is the chemical potential of oxygen at given T (K) and P (bar) conditions, $G^0 O_{2,\text{pure}}{}^{T,1\text{bar}}$ represents reference Gibbs energy of pure oxygen gas at fixed T (K) and 1 bar, and R is the ideal gas constant with a value of 8.3145 J/(mol·K). Calculations were performed using the Perple_X subprograms Werami and Frendly (reference). The fO_2 value relative to the fayalite-magnetite-quartz buffer (FMQ) is the difference in oxygen fugacity between the system and pure FMQ buffer (1):

$$\Delta FMQ = (\mu O_{2,\text{rock}} - \mu O_{2,\text{FMQ}})/(2.303RT)$$

where $\mu O_{2,\text{rock}}$ and $\mu O_{2,\text{FMQ}}$ are the partial molar Gibbs energy of oxygen for the modeled system and hypothetical FMQ buffer, respectively. In the Perple_X program, the fluid fractionation model is a Rayleigh fractionation process.

Error analysis of thermodynamic predictions

The largest uncertainty of the calculations performed here is the source of the thermodynamic parameters for minerals and aqueous species and the extrapolation capability of the thermodynamic models to the high temperatures and pressures of subduction zones. Thermodynamic data for minerals used for phase equilibria modeling stem from the revised Holland and Powell mineral database, which has recently been extended to lower mantle conditions, up to 300 kbar and 2000 °C (2). According to those authors themselves, the inherent uncertainties of this data set, when using the Thermocalc program for calculating mineral stability fields at 6.4 kbar and 1000 °C - the conditions relevant to the conditions of this study, are typically ±0.3 kbar and ±20 °C. Thermodynamic parameters for major aqueous species in our modeling stem from the recent Deep-Earth-Water (DEW) dataset (3), within the framework of the revised Helgeson-Kirkham-Flowers (HKF) equation of state, which is considered to be valid up to 60 kbar and 1000 °C. In addition, Galvez et al. (4) concluded that the discrepancies between the DEW database and the previous HKF-model datasets of Supcrt92 for major fluid constituents in terms of species concentration are typically no more than 10% at >200 °C. Differences between predicted solubility for major oxide and silicate minerals and experimental results do not generally exceed ± 0.5 log units in solute concentration (3, 5). Thus, computational errors of major solute concentrations in our models are < ± 0.5 log unit.

The uncertainties of gold solubility predictions are dominantly from the equilibrium constant of the reaction $Au(HS)_2^- + S_3^- = Au(HS)S_3^- + HS^-$ coupled with the thermodynamic data of S_3^-,H_2S and HS^-. Sulfur aqueous species and gold complexes are described by the HKF model (Table S5) using the same data sources for most major species as the DEW model, thereby ensuring internal consistency and allowing partial error cancellation. The uncertainties of Au solubility predictions in the $Au\text{-}H_2S\text{-}S_3^-$ system as analyzed in detail in ref. (6) do not exceed 0.5 log unit at < 700 °C and 1–10 kbar; they approach 1 log unit at higher temperatures and pressures. Furthermore, these parameters of the Au-S complexes are validated by predictions of Au solubility in magmatic and metamorphic fluids above 600 °C, whose results are comparable with Au content data of natural fluid inclusions (6, 7). The thermodynamic parameters of $AuCl_2^-$ were adopted here from the revised HKF model applied to a large set of most robust experimental data (8), ensuring concentration predictions for $AuCl_2^-$ within < 0.3 log unit up 1000 °C and 5 kbar. Consequently, the thermodynamic predictions of Au solubility at 15 kbar, 600 °C are judged to be reliable within the presently estimated uncertainty above. As shown in Fig. S6, we also predicted similar Au aqueous speciation and concentration trends at 700 °C and 800 °C, 15 kbar. Even though, the predicted absolute concentrations of $Au(HS)_2^-$ and $Au(HS)S_3^-$ are about 1 log unit lower than those at 600 °C, 15 kbar, (Fig. S6), they do remain within the expected error margins. We, however, caution that the presently available thermodynamic parameters for Au complexes should be used with prudence above 600 °C in the absence of direct experimental measurements. We should emphasize that our Au solubility predictions are pessimistic in light of the potential existence of other soluble gold complexes, for example, with the S_2^- ion, for which no numerical data are currently available. Inclusion of such and other complexes into consideration in future is expected to further strengthen our model of enhanced Au mobilization across the metasomatized mantle wedge.

Errors on the predicted Au contents in aqueous fluid and silicate melt during partial melting dominantly source from the sulfur solubility and Au partition coefficient data. In our models, sulfur solubilities in melt and fluid are determined by interpolation of available experimental data. These experiments were conducted at 10–20 kbar, 1000–1300 °C and redox conditions from ΔFMQ–3 to ΔFMQ+4, covering the stability fields of monosulfide solid solution (MSS), sulfide liquid (SL), and anhydrite ($CaSO_4$) (9-12). These experimental data have an analytical uncertainty of <10%, as reported in the original studies, which propagates to a prediction error of ±10% for sulfur concentrations in our model. Numerous high-temperature, high-pressure experiments investigated the Au partitioning between sulfide (MSS and SL) and silicate melts and reported $D_{Au}^{MSS/melt}$ values of 50–300 and $D_{Au}^{SL/melt}$ values of 1000–10000 (11-13). The partition coefficient of Au between aqueous fluid and silicate melt is a strong function of sulfur concentration and oxygen fugacity; available data spanning over a range of 10–200 for $D_{Au}^{fluid/melt}$ (14). We thus adopted $D_{Au}^{SL/melt}$ of 2200, $D_{Au}^{MSS/melt}$ of 200, and $D_{Au}^{fluid/melt}$ of 100 for predictions of Au concentrations in the aqueous fluid and hydrous silicate melt, implying a pessimistic prediction uncertainty of < 0.5 log units. To simplify the mass balance calculations, a constant fraction of fluid phase is assumed within the fluid-melt-rock system. However, the free-fluid content may be significantly influenced by pressure, temperature, H_2O solubility and melting degree in natural systems. It thus should be emphasized that our model data provide a tentative estimation of gold extraction during fluid-present melting of metasomatized mantle, in the absence of empirical or thermodynamic models that could effectively couple chemical reactions and physical transport of aqueous fluids and silicate melts.

Values of pH of slab-derived fluid in equilibrium with mantle peridotite

The pH value of the aqueous fluid controls the transport and enrichment of many metals and volatiles during mantle metasomatism. Here, the fluid alkalinity (ΔpH) is employed to distinguish nominally acidic (ΔpH < 0) and alkaline (ΔpH > 0) compositions, as defined by ΔpH = pH – pH_n. In this equation, pH_n is so called the pH of the neutrality point of pure water at the condition of $\alpha_{H^+} = \alpha_{OH^-}$:

$$pH_n = 0.5 \times [pK_W - \log_{10}(\alpha_{H_2O})]$$

where pK_W and $\log_{10}(\alpha_{H_2O})$ are the ionization constant and activity of water. We designed two infiltration scenarios to test the role of fluid-rock interaction introduced by mantle metasomatism on pH of slab-derived fluid at 2.4 GPa, 1000 °C and 3.3 GPa, 1000 °C. All calculations of fluid pH were performed in the Perple_X subprogram Werami. Our model predicts a nominally alkaline pH range (absolute pH = 5.0–6.0, ΔpH = 1.6–2.5) of the mantle-wedge fluid and a decrease of pH with increasing the fluid/rock ratio, both for hot and cold subduction models (Fig. S7A and B). Previous thermodynamic models also predicted that mantle peridotite is capable of buffering the fluid ΔpH values between 0.5 and 2.5 at fore-arc and sub-arc P-T conditions (15). Fluid inclusion data from mantle xenoliths indicate salinity of 5±1 wt.% NaCl equivalent in the subduction fluid (16). The addition of chloride is expected to further decrease the fluid ΔpH towards neutrality as also thermodynamically predicted in ref. (15). In conclusion, the pH of mantle-wedge fluids is confined to a mildly alkaline range, where the $Au(HS)S_3^-$ and $Au(HS)_2^-$ are favored and Au solubility attains ppm-level concentrations(Fig. S7C).

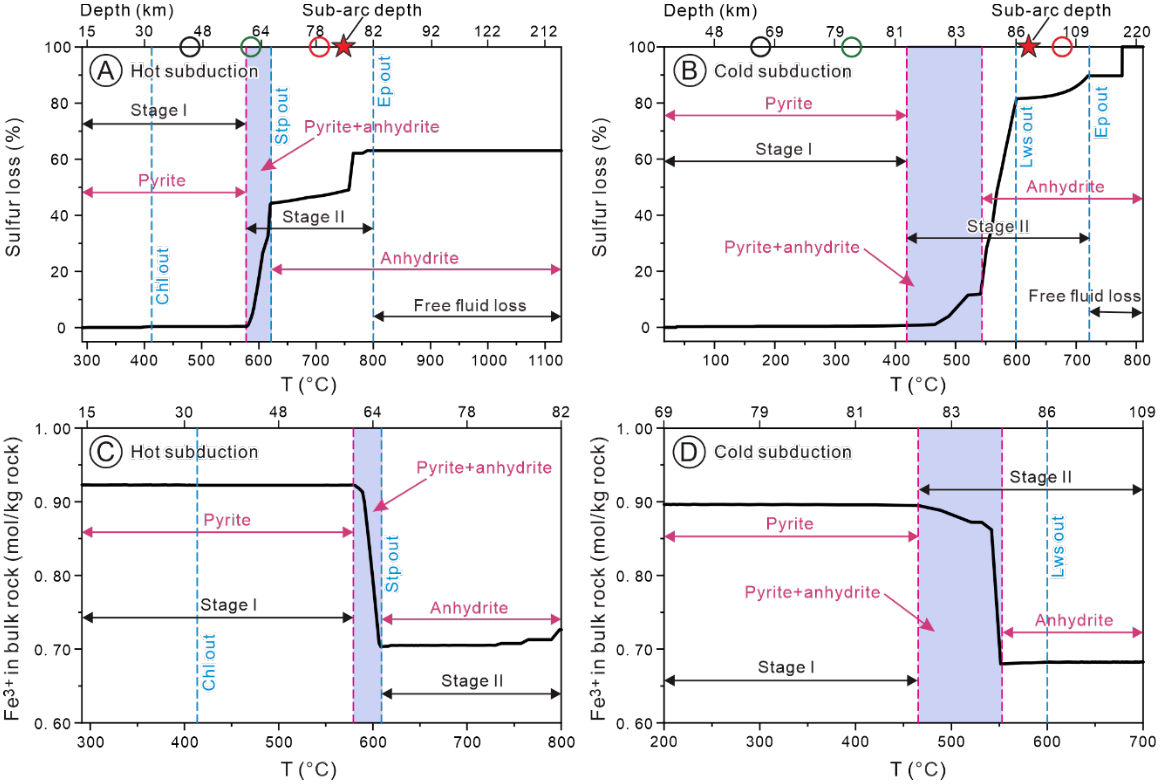

Fig. S1. Variations in sulfur loss and Fe^{3+} contents in bulk rock system along the hot and cold subduction P-T paths. (**A** and **B**) Plots of degree of sulfur loss (in wt.% relative to the initial value) vs. temperature and depth of the slab top along the hot (**A**) and cold (**B**) subduction paths. (**C** and **D**) Variations in Fe^{3+} contents of the bulk rock system. Pink horizontal double-head arrows and blue-shaded regions display the variations of S-bearing mineral assemblages. Black horizontal double-head arrows mark two dehydration stage. The vertical blue dashed lines mark the temperature conditions of complete breakdown of the dominant hydrous phases. Note an obvious trend of bulk rock Fe^{3+} contents decrease with the transition from pyrite to anhydrite.

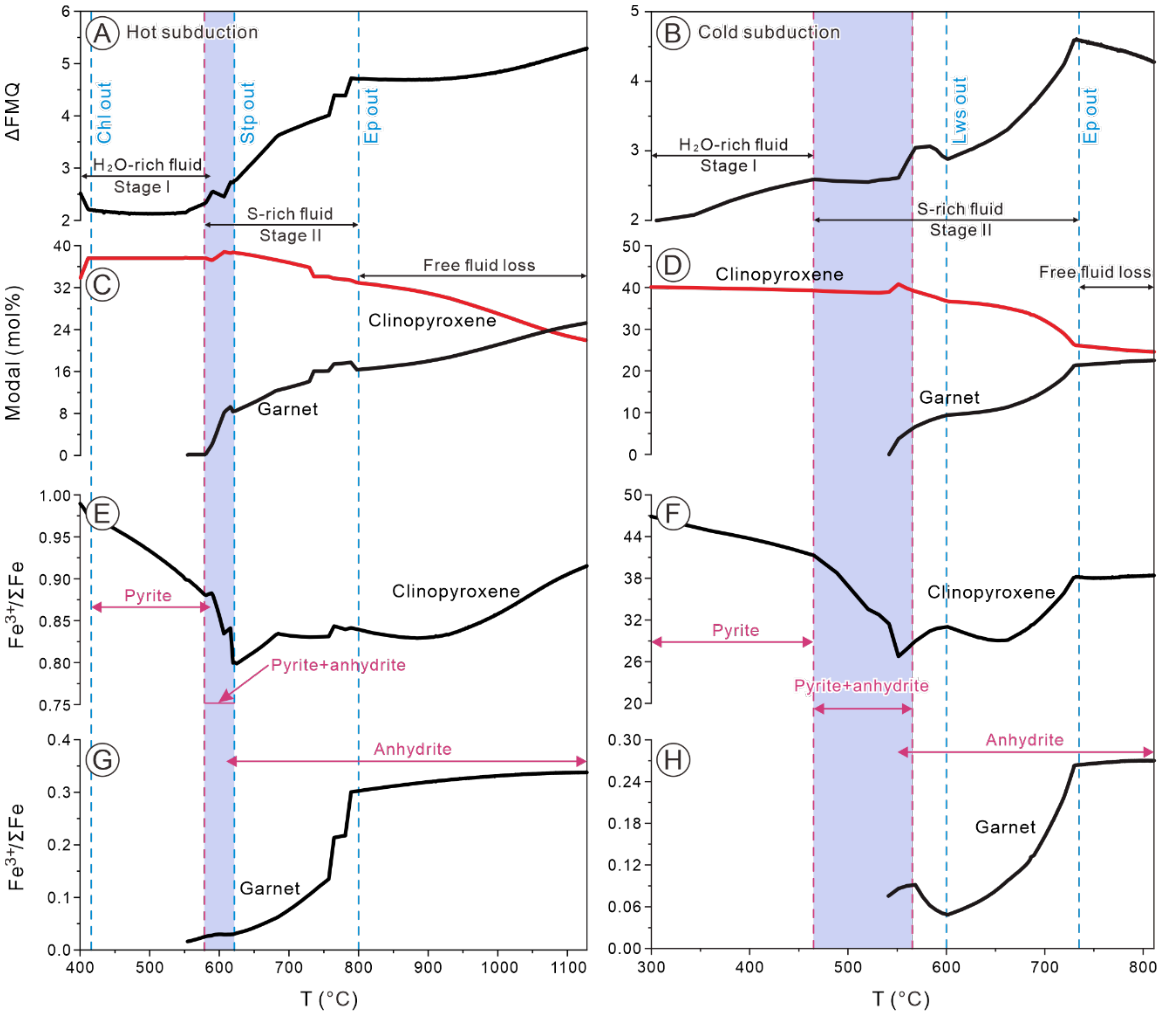

Fig. S2. Prograde devolatilization evolution of AOC along hot and cold subduction geotherms. (**A** and **B**) Oxygen fugacity variation of the AOC system along the hot and cold subduction P-T path during devolatilization processes. (**C** and **D**) Mole proportions of clinopyroxene and garnet at each P-T point. (**E** and **F**) The effect of fluid release on $Fe^{3+}/\Sigma Fe$ ratio of clinopyroxene along hot and cold subduction paths. (**G** and **H**) Progressive variation along subduction P-T path of the $Fe^{3+}/\Sigma Fe$ ratios in garnet. The vertical blue dashed lines mark the temperature conditions of complete decomposition of the dominant hydrous minerals. Pink horizontal double-head arrows show the stability fields of S-bearing minerals. Blue filled region illustrates the temperature interval of pyrite-anhydrite coexistence. Two dehydration stages are marked by black horizontal double-head arrows.

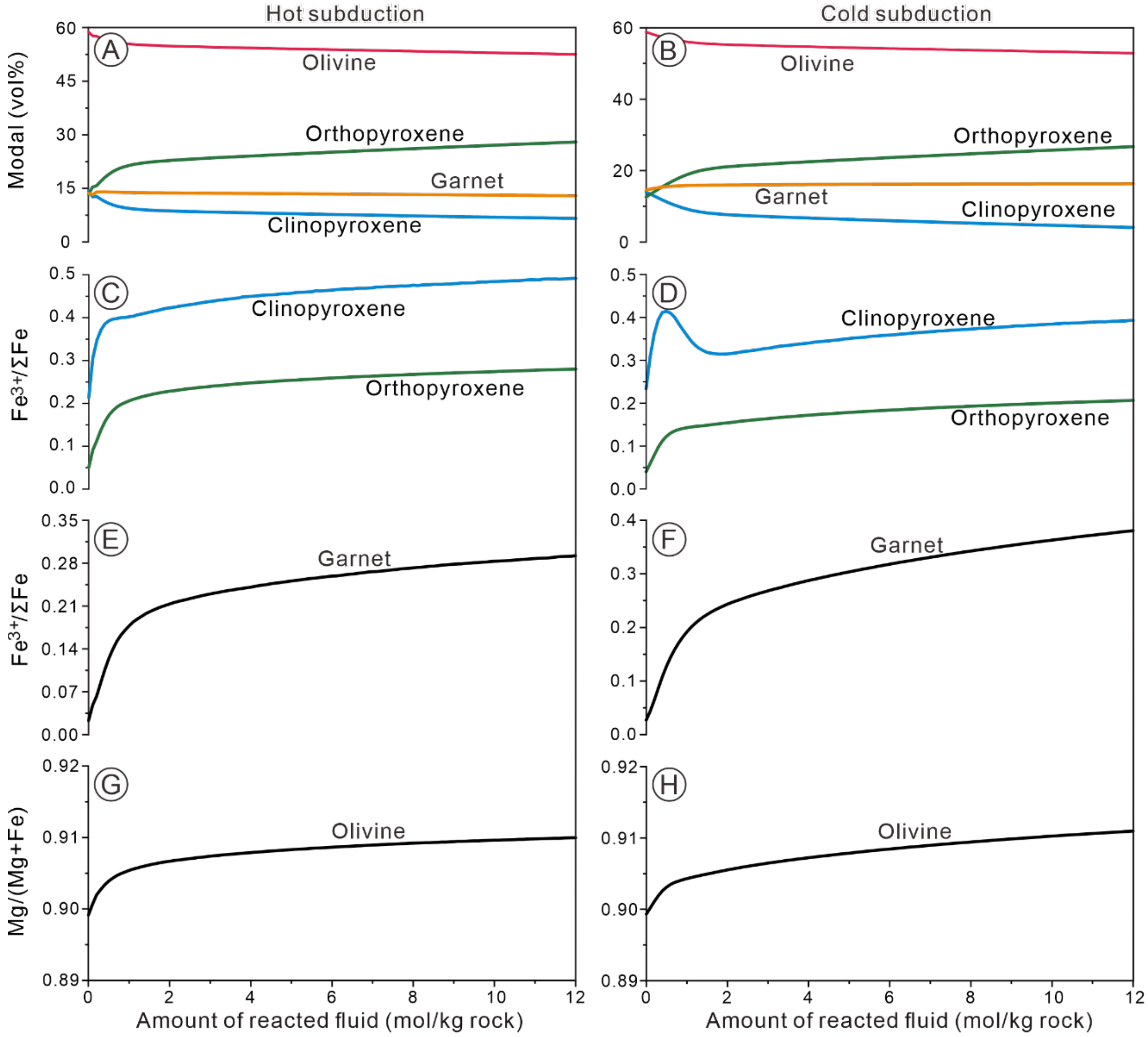

Fig. S3. Variations in the composition of depleted mantle peridotite metasomatized by an AOC-derived aqueous fluid. (**A** and **B**) Modal abundances (in vol.%) of primary minerals of modeled mantle peridotite. (**C–H**) Isothermal and isobaric evolutions with fluid infiltration of the $Fe^{3+}/\Sigma Fe$ in clinopyroxene, orthopyroxene (**C** and **D**) and garnet (**E** and **F**), and Mg/(Mg+Fe) ratios in olivine (**G** and **H**).

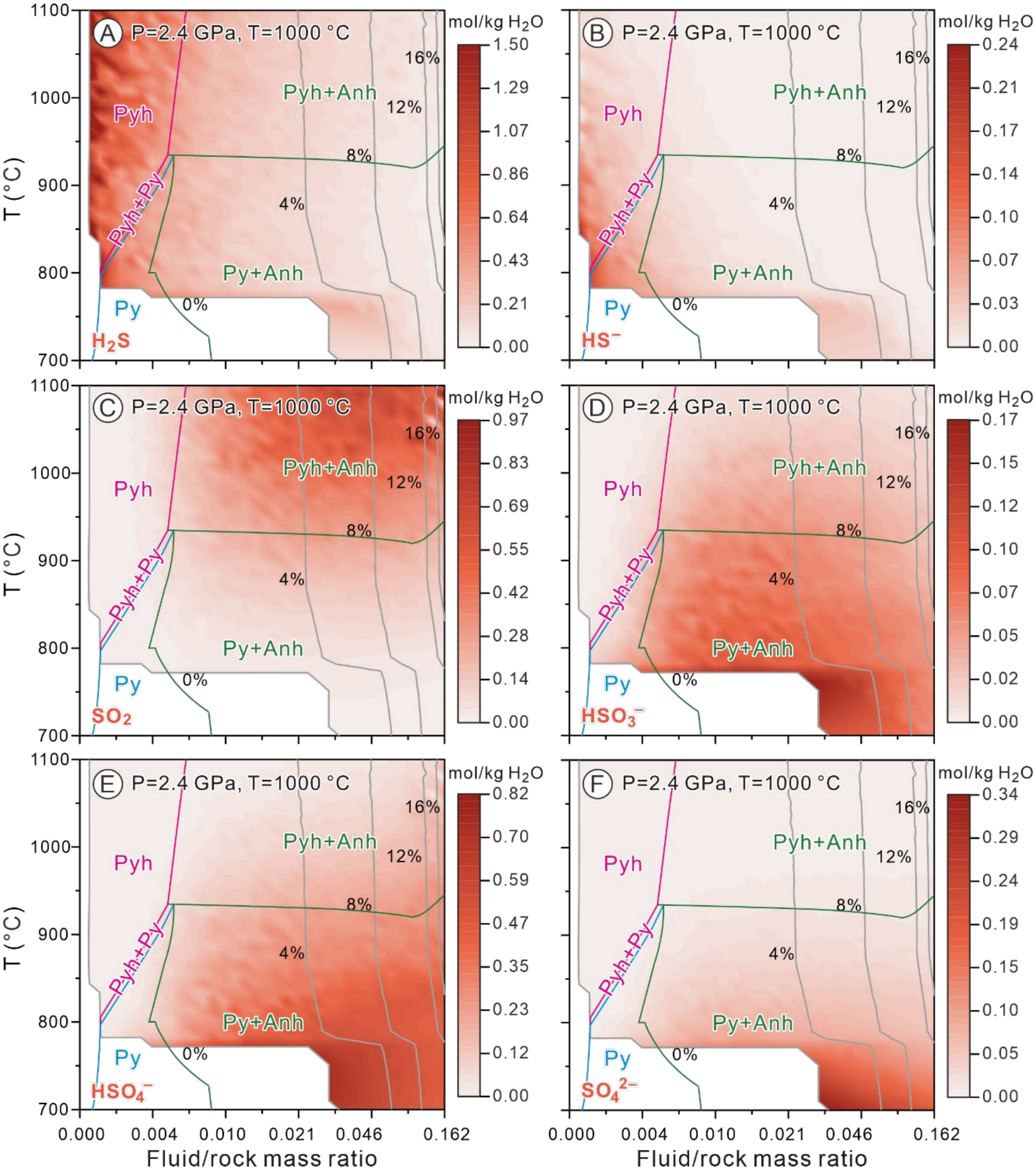

Fig. S4. Equilibrium abundances of dominant sulfur species in slab-derived fluid after its reaction with depleted mantle peridotite calculated for the hot subduction model. Contour maps of the concentrations of reduced (**A** and **B**) and oxidized (**C–F**) sulfur species in mol/kg shown by color bars at the right side of each panel. Color curves outline the phase boundaries of S-bearing mineral assemblages. Gray contours state in weight percent (wt.%) of aqueous fluid in the whole system after fluid reaction with mantle peridotite (note non-linear scale for the fluid/rock mass ratio).

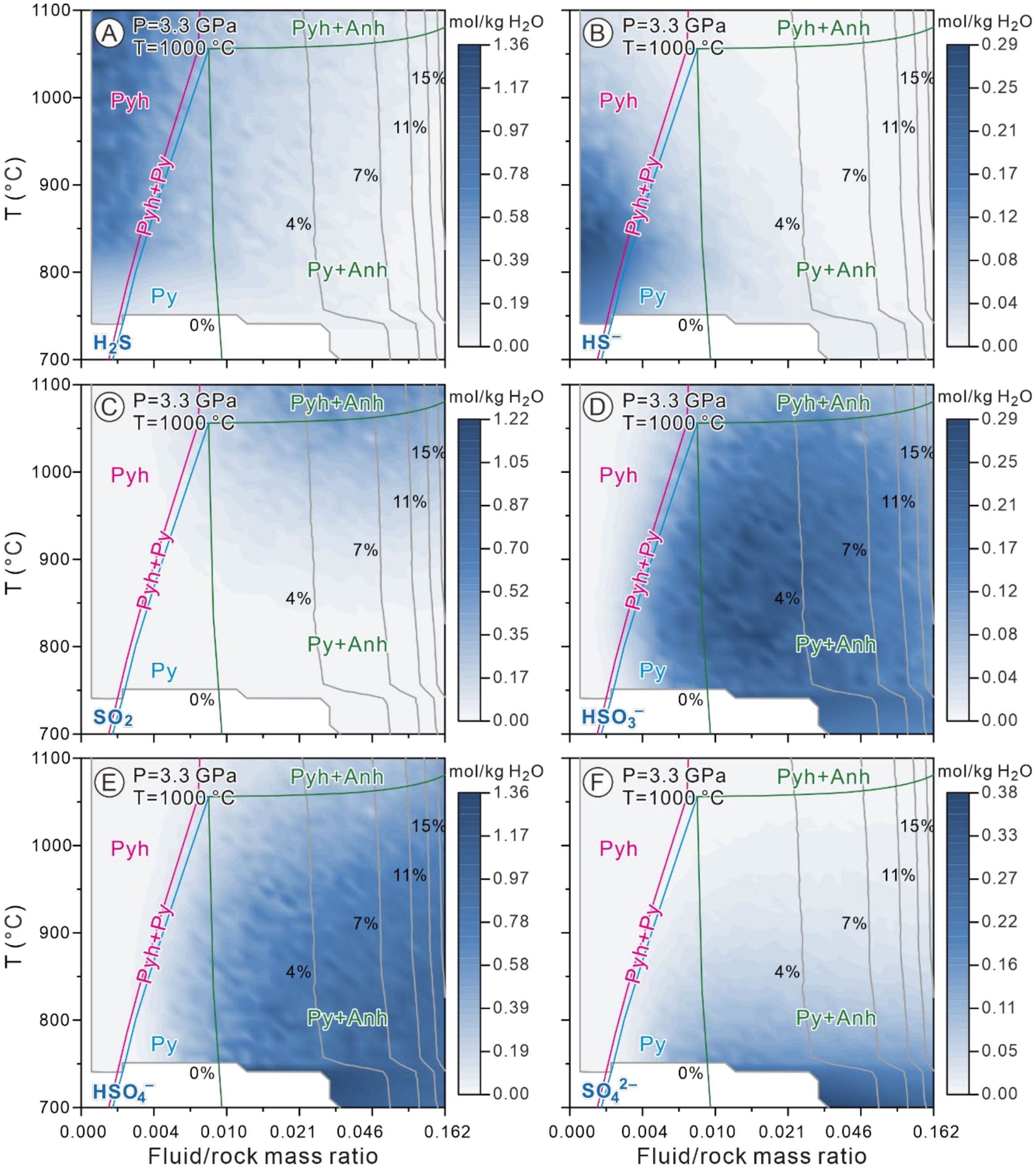

Fig. S5. Equilibrium abundances of dominant sulfur species in slab-derived fluid after its reaction with depleted mantle peridotite calculated for the cold subduction model. Contour maps of the concentrations of reduced (**A** and **B**) and oxidized (**C–F**) sulfur species in mol/kg shown by color bars at the right side of each panel. Color curves outline the phase boundaries of S-bearing mineral assemblages. Gray contours in weight percent (wt.%) of aqueous fluid in the whole system after fluid reaction with mantle peridotite (non-linear scale for the fluid/rock ratios).

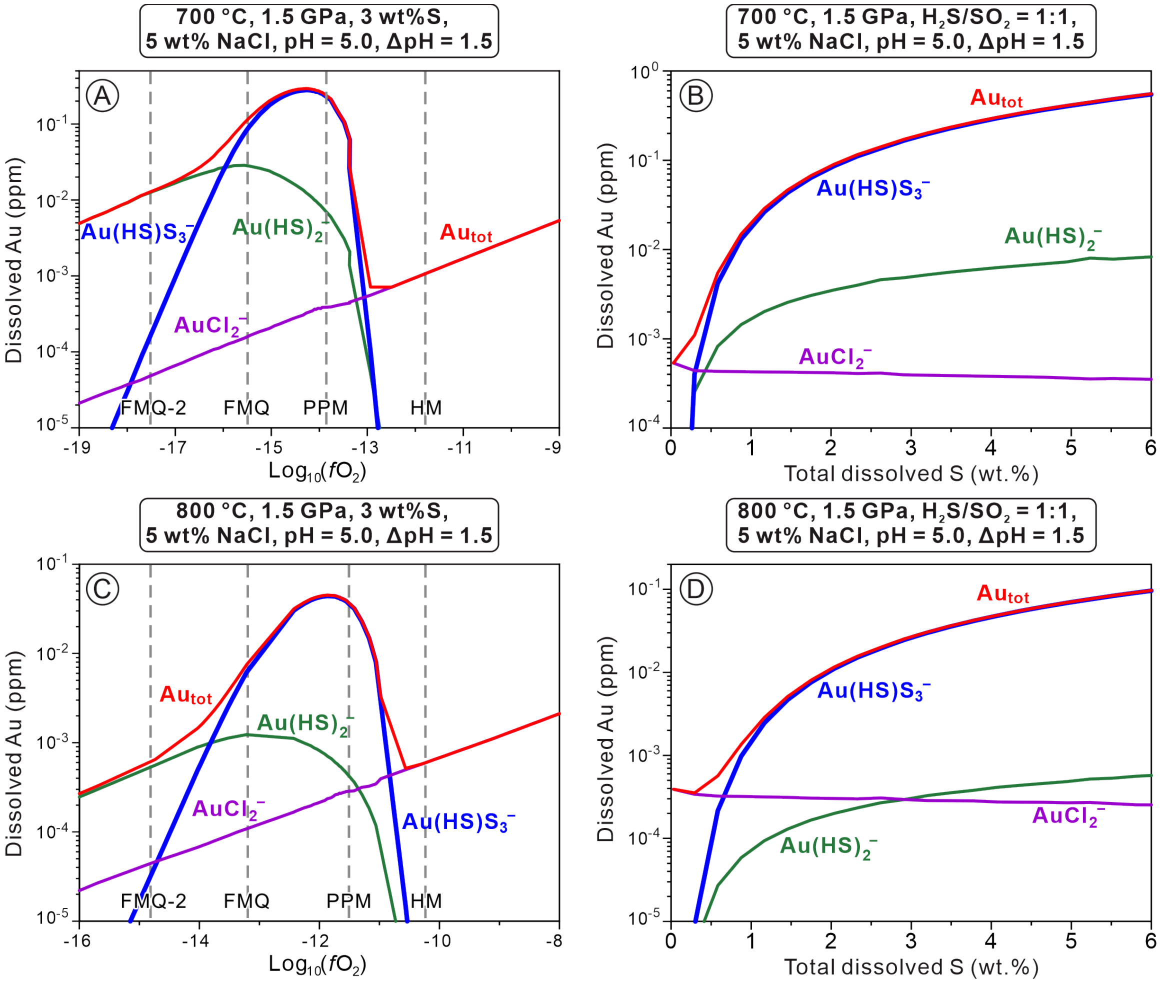

Fig. S6. Gold concentration and speciation in slab-derived fluid in equilibrium with a native Au-bearing mantle rock as a function of oxygen fugacity and total dissolved S content at 1.5 GPa and 700 °C (A–B) and 800 °C (C–D). The fluid pH is buffered at ~5 by the olivine-pyroxene-garnet mantle rock assemblage with fluid/rock mass ratio of 0.1. The vertical gray dashed lines in (**A**) and (**C**) indicate the fO_2 values corresponding to the fayalite-magnetite-quartz (FMQ), pyrite-pyrrhotite-magnetite (PPM) and hematite-magnetite (HM) conventional redox buffers. The H_2S-SO_2 equilibrium in the fluid imposes oxygen fugacity in panels (**B**) and (**D**).

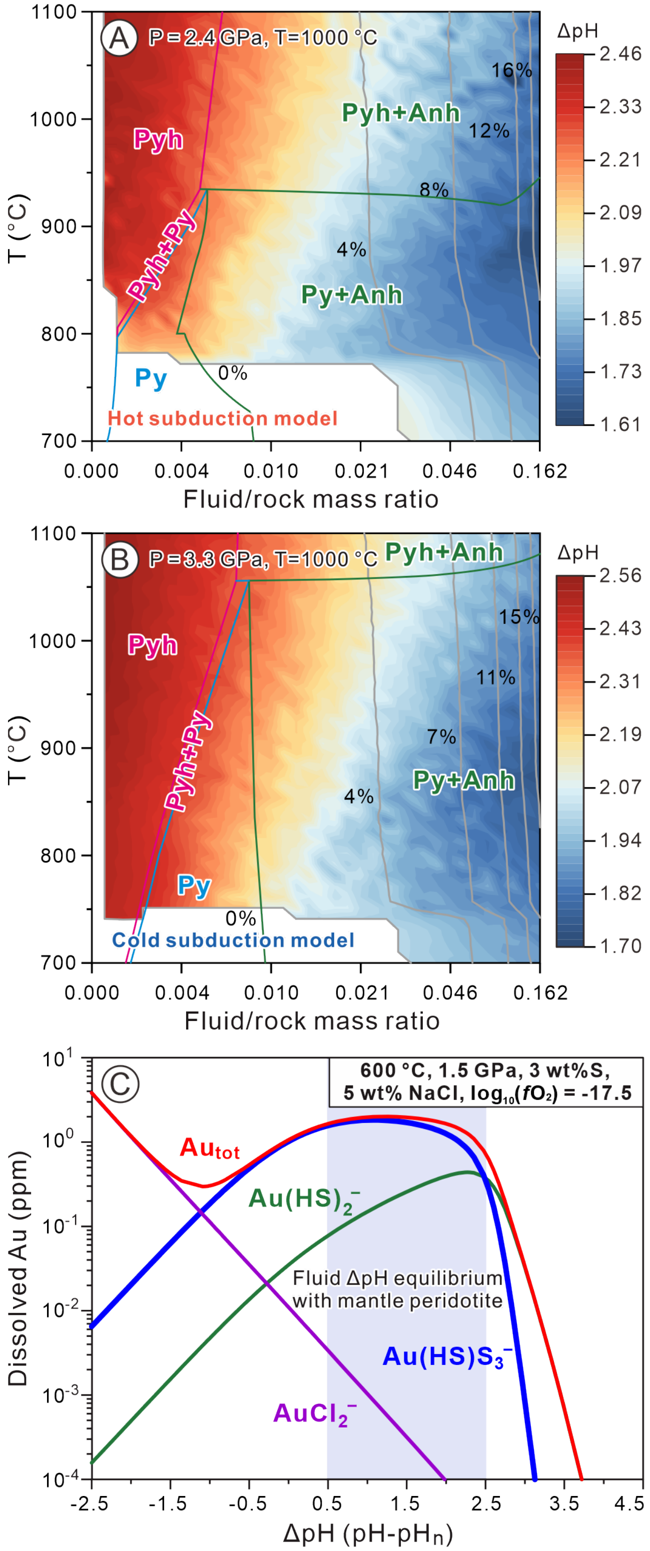

Fig. S7. ΔpH of slab-derived fluid after reaction with mantle peridotite (A and B) and its effect on Au solubility and speciation (C). Color contour maps in (A) and (B) plotted for the stable sulfur-bearing mineral assemblages indicate the acidic or alkaline character of the slab-derived fluid after interaction with peridotite as a function of the fluid/rock mass ratio. The gray-line contours indicate the weight percentage (wt.%) of aqueous fluid after reaction with mantle peridotite. (C) Gold solubility and speciation as a function of the fluid ΔpH at 1.5 GPa, 700 °C and $\log_{10}(fO_2$, bar) = –17.5. The vertical blue-shaded region encompasses the typical ΔpH values (from 0.5 to 2.5) of mantle fluid predicted by fluid-rock phase equilibrium modeling in this study and ref. (4).

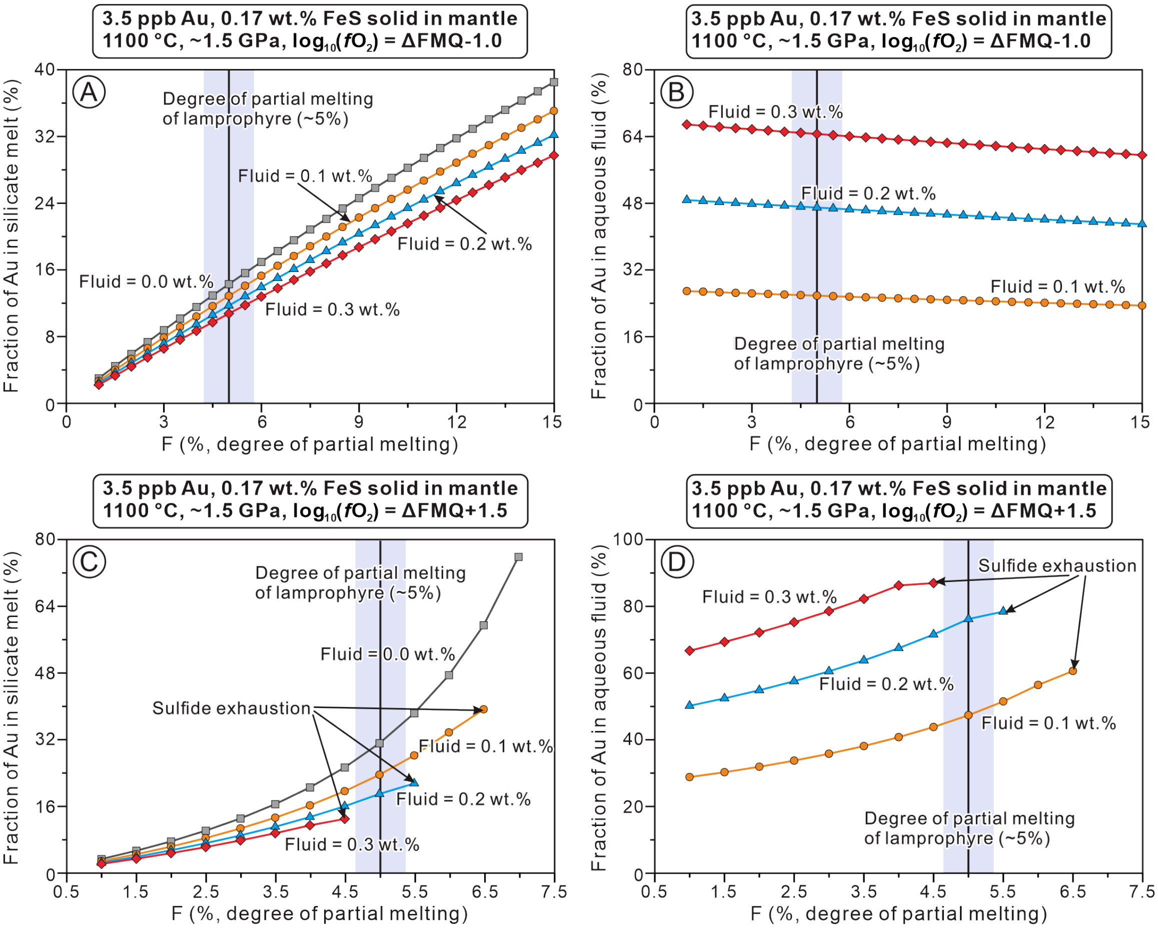

Fig. S8. Predicted gold fractions in the coexisting aqueous fluid and mantle silicate melt at low-temperature hydrous mantle melting in the presence of MSS. Modeled Au relative amounts in fluid and silicate melts at fO_2 of ΔFMQ–1.0 (A and B) and ΔFMQ+1.5 (**C** and **D**). The vertical, blue-shaded region defines a low-degree melting range, typically of 5% for lamprophyre marked by vertical black solid line. Fluid proportions indicated in all panels represent the assumed fraction of the free aqueous fluid of the system.

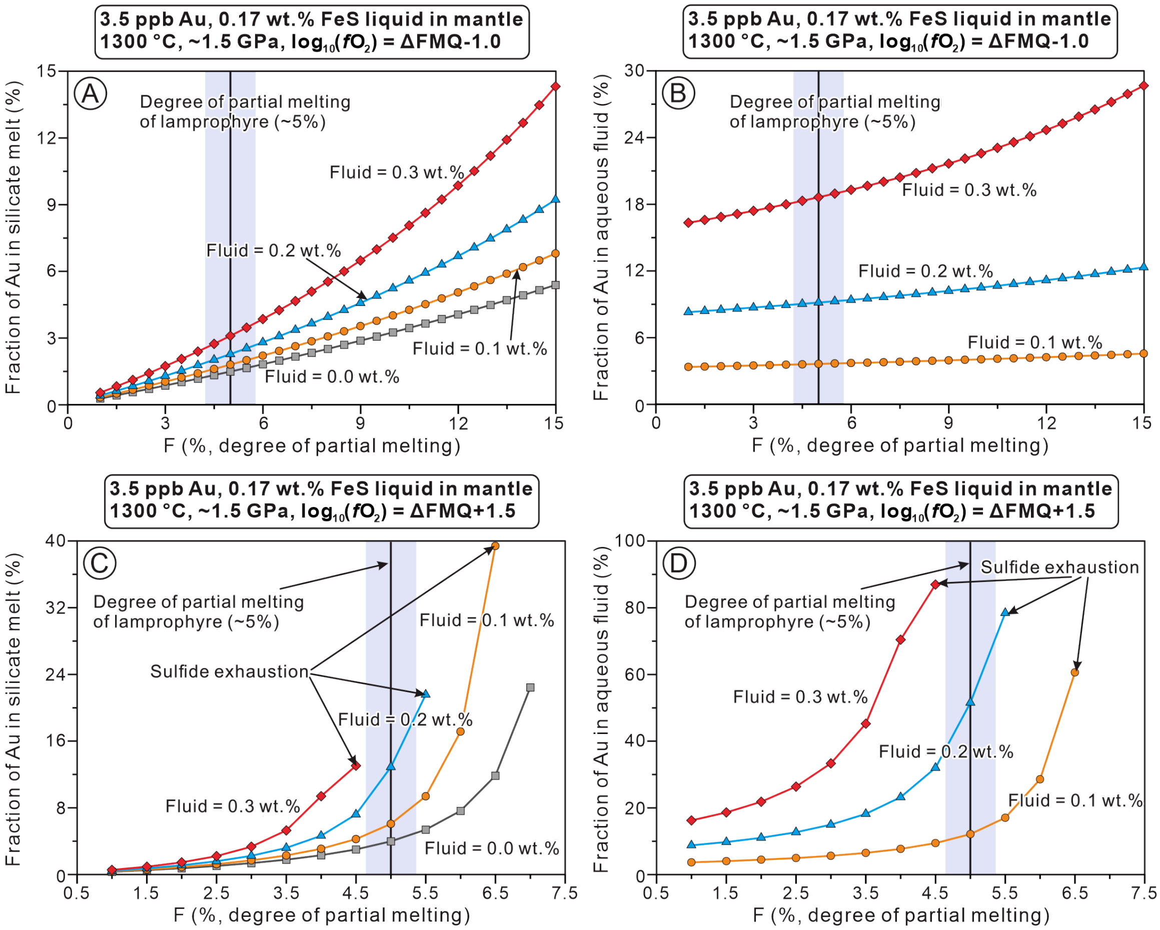

Fig. S9. Predicted gold relative amounts in the coexisting aqueous fluid and mantle silicate melt at high-temperature hydrous melting in the presence of sulfide liquid, at fO_2 of ΔFMQ–1.0 **(A** and **B)** and ΔFMQ+1.5 (**C** and **D**). The vertical, blue-shaded region defines a low-degree melting range, typically of 5% for lamprophyre marked by vertical black solid line. Fluid proportions indicated in all panels represent the assumed fraction of the free aqueous fluid of the system.

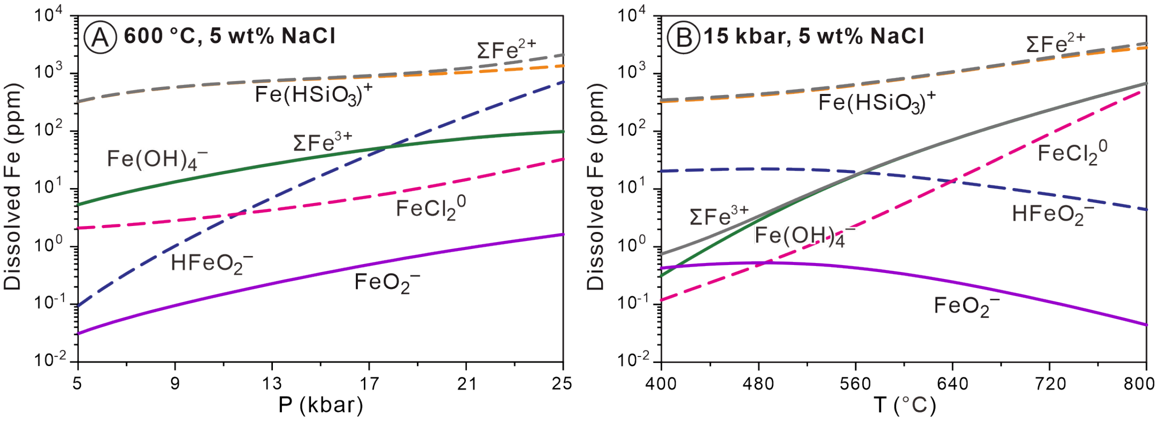

Fig. S10. Concentrations of major iron-bearing aqueous species in slab-derived fluid as functions of pressure (A) and temperature (B). Iron solubility and speciation are calculated by equilibrating a H_2O-NaCl fluid with hematite and magnetite. The oxygen fugacity and fluid pH are buffered by the hematite-magnetite and quartz-muscovite-feldspar mineral assemblages, respectively, as representative of the slab crustal-rock mineralogy. It can be seen that the concentrations of ferrous iron complexes are 1–2 orders of magnitude higher than those of ferric iron. Thermodynamic properties of aqueous species and minerals are from Table S5. Note in panel A the concertation curves of $Fe(OH)_4^-$ and ΣFe^{3+} are coincident.

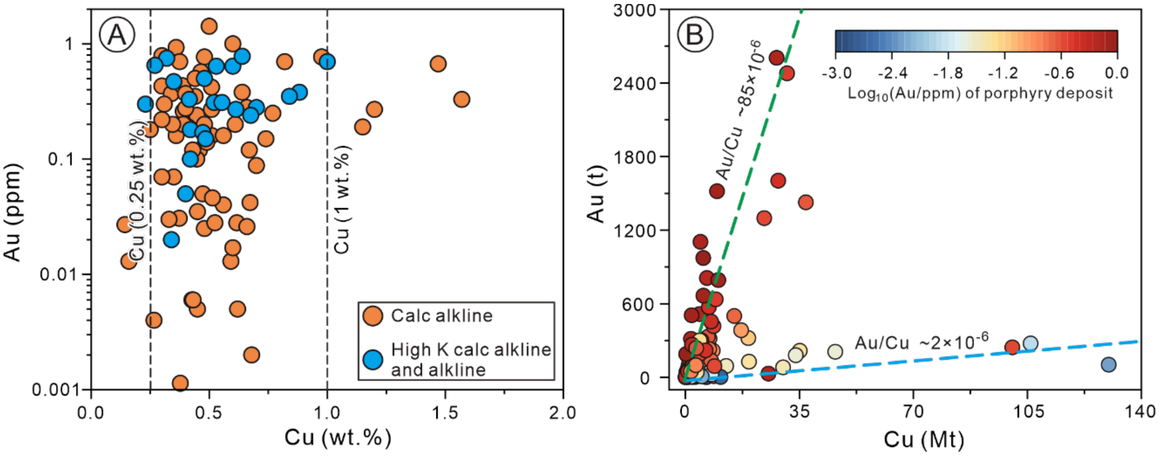

Fig. S11. Metal grades of major porphyry Cu(-Au) deposits. (**A**) Plot of average grade of Au (ppm) vs. Cu (wt.%) of porphyry Au-Cu deposits. (**B**) Au (t) vs. Cu (Mt) diagram displaying two distinct groups of porphyry Cu(-Au) deposits, a Cu-rich (along the blue line) and an Au-rich (along the green line). Data from Table S6.

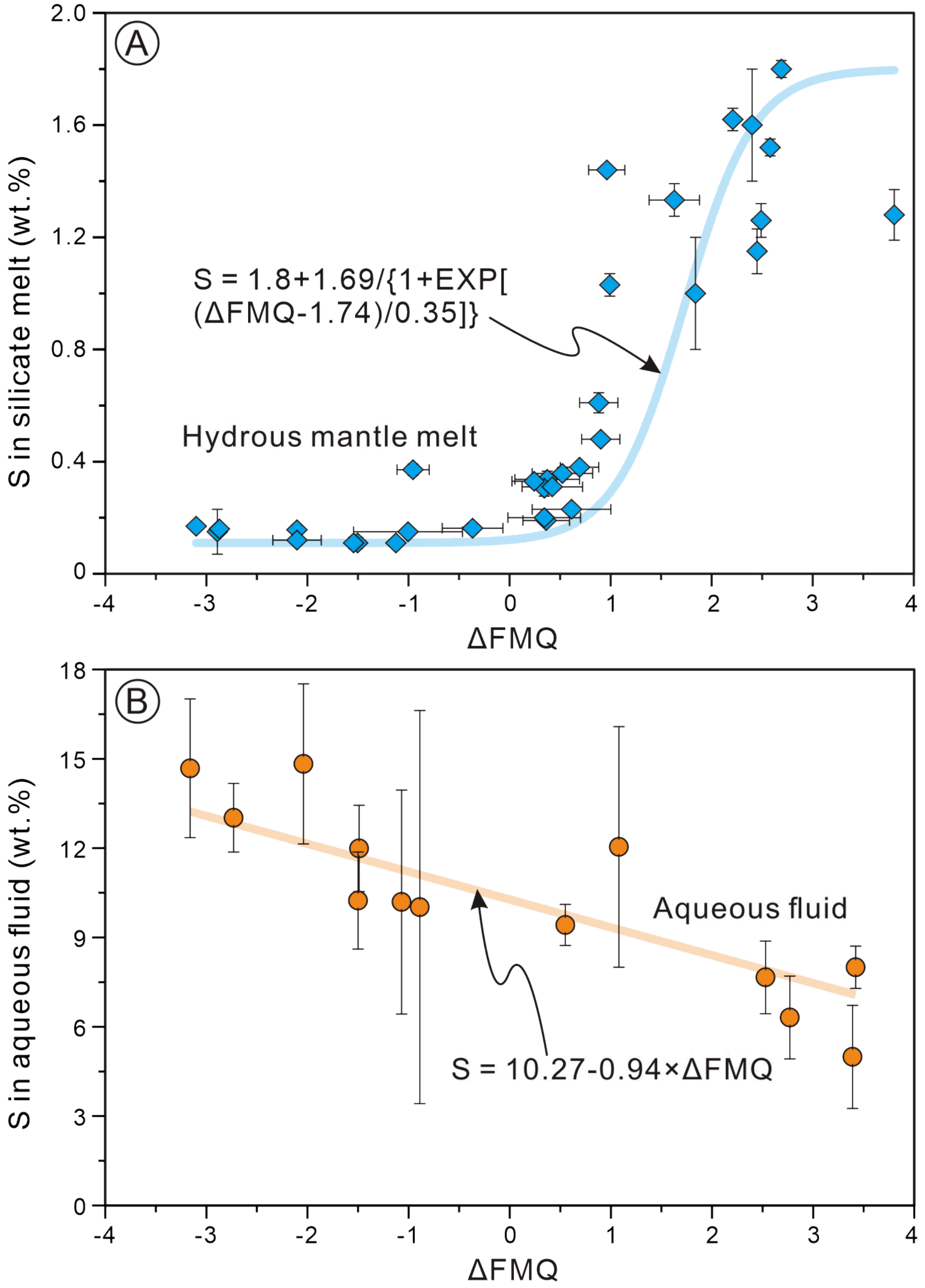

Fig. S12. Experimentally measured sulfur solubility in hydrous mantle silicate melt (A) and aqueous fluid (B) at different fO2 conditions (relative to FMQ), at 1–2 GPa, 1000–1300 °C, and at saturation with iron sulfide, anhydrite, or both solids (depending on fO2). Points are literature experimental data whereas the curves are empirical least-square fits to those data used in the Au and S partitioning modeling of this study. It can be seen that sulfur concentrations in the silicate melt increase with increasing fO_2, in particular at the sulfide-sulfate transition and; whereas those in aqueous fluid are much less affected by fO2, with only a slight decrease; they remain 5 to 20 times higher than in the coexisting hydrous melt. All experimental data sources are from refs. (9-12 and 17).

Table S1. **Bulk rock compositions of the altered oceanic crust and input data for the devolatilization model along hot and cold subduction zones.** The chemical compositions are modified from Kelley et al.(18) and Padrón-Navarta et al.(19) with $Fe^{3+}/\Sigma Fe = 0.51$. The contents of volatiles in AOC are from Evans (20), and carbon is given as CO_2. In addition, 66% sulfur of AOC is considered as pyrite and the remainder as anhydrite (20). Water contents of AOC are given by assuming H_2O saturation at the first P-T point for hot and cold subduction zones.

Whole rock (wt.%)		**Input data (mol/kg)**		**Whole rock (wt.%)**		**Input data (mol/kg)**	
For hot subduction path				For cold subduction path			
SiO_2	47.85	Si	7.9110	SiO_2	46.42	Si	7.6913
Al_2O_3	11.71	Al	2.2820	Al_2O_3	11.36	Al	2.2186
FeO_t	11.99	Fe	1.6581	FeO_t	11.64	Fe	1.6121
MgO	6.05	Mg	1.4901	MgO	5.86	Mg	1.4487
CaO	12.67	Ca	2.2432	CaO	12.29	Ca	2.1809
Na_2O	2.24	Na	0.7165	Na_2O	2.17	Na	0.6966
K_2O	0.60	K	0.1271	K_2O	0.58	K	0.1236
H_2O	4.54	H_2	2.5034	H_2O	7.40	H_2	3.9755
CO_2	2.25	C	0.5064	CO_2	2.18	C	0.4923
S	0.10	S_2	0.0160	S	0.10	S_2	0.0156
Total	100.00	O_2	14.5099	Total	100.00	O_2	14.8777

Table S2. Chemical compositions of modeled mantle peridotite and input rock data for the mantle infiltration model. Compositions of depleted mantle are from Salters et al.(21). The ferric iron to total iron ratio is 0.03 according to Canil et al.(22). The volatiles of mantle peridotite are not included in the modelling due to their too low concentrations.

Whole rock (wt.%)		**Input data (mol/kg)**	
SiO_2	45.23	Si	7.5277
Al_2O_3	4.31	Al	0.8457
FeO_t	8.13	Fe	1.1313
MgO	38.50	Mg	9.5528
CaO	3.53	Ca	0.6286
Na_2O	0.29	Na	0.0943
Total	100.00	O_2	13.8476

Table S3. Fluid elemental compositions (in moles of chemical element) extracted from the devolatilization model at different subduction depths and used for computing mantle infiltration models. The fluid compositions are normalized to 2 moles of hydrogen (H).

Hot subduction model				**Cold subduction model**			
Depth, km	45	63	80	Depth, km	65	80	100
Si	0.0035	0.0094	0.0238	Si	0.0238	0.0018	0.0025
Al	0.0003	0.0007	0.0014	Al	0.0012	0.0000	0.0000
Fe	0.0004	0.0018	0.0024	Fe	0.0016	0.0001	0.0000
Mg	0.0004	0.0007	0.0010	Mg	0.0007	0.0001	0.0000
Ca	0.0002	0.0008	0.0042	Ca	0.0074	0.0018	0.0007
Na	0.0107	0.0191	0.0324	Na	0.0304	0.0011	0.0023
K	0.0001	0.0017	0.0079	K	0.0078	0.0021	0.0006
H_2	1.0000	1.0000	1.0000	H_2	1.0000	1.0000	1.0000
C	0.0197	0.0551	0.1980	C	0.0935	0.0029	0.0012
S_2	0.0002	0.0017	0.0078	S_2	0.0081	0.0007	0.0000
O_2	0.5268	0.5761	0.7595	O_2	0.6566	0.5085	0.5049

Table S4. The detailed parameters and abbreviations of solid solution models considered in the present study. For mantle metasomatism modeling, we considered solid solution models of biotite, clinopyroxene, garnet and orthopyroxene specifically calibrated for the mantle conditions.

Phase	**Abbreviation**	**Reference**	**Notes**
Amphibole	**cAmph(G)**	Green et al.(23)	
Biotite	**Bi(HGP)**	Holland et al.(24)	For mantle peridotite
Chlorite	**Chl(W)**	White et al.(25)	
Clinopyroxene	**Omph(GHP)**	Green et al.(26)	
Clinopyroxene	**Cpx(HGP)**	Holland et al.(24)	For mantle peridotite
Dolomite	**Do(HP)**	Holland and Powell(27)	
Epidote	**Ep(HP11)**	Holland and Powell(28)	
Feldspar	**feldspar**	Fuhrman and Lindsley(29)	
Garnet	**Gt(WPH)**	White et al.(25)	
Garnet	**Gt(HGP)**	Holland et al.(24)	For mantle peridotite
Magnesite	**M(HP)**	Holland and Powell(27)	
Muscovite	**Mica(W)**	White et al.(25)	
Orthopyroxene	**Opx(HGP)**	Holland et al.(24)	For mantle peridotite
Pumpellyite	**Pu**	Massonne and Willner(30)	
Pyrrhotite	**Po(HP)**	White et al.(25)	
Stilpnomelane	**Stlp**	Massonne and Willner(30)	
Fluid	**COH-Fluid+**	Connolly and Galvez(31)	

Table S5. Data sources of the thermodynamic properties of aqueous species and mineral phases selected for geochemical modeling of gold, sulfur and iron solubility in slab-derived fluid. These properties are described by the revised Helgeson-Kirkham-Flowers equation of state. Mineral phases such as orthopyroxene, clinopyroxene, olivine, and garnet are approximated by ideal solid solution models between their indicated end-members in the HCh package for simplicity; others are considered as pure phases.

Aqueous species and mineral phases	**Data source**
Aqueous species	
H_2O, H^+, OH^-, Cl^-, Na^+, $NaCl^0$, $NaOH^0$, KCl^0, K^+, KOH^0, KSO_4^-, $KHSO_4^0$, $NaHSO_4^0$, HS^-, $HS_2O_3^-$, $S_2O_3^{2-}$, HSO_3^-, SO_3^{2-}, HSO_4^-, SO_4^{2-}, Ca^{2+}, $CaOH^+$, $CaSO_4$, $CaCl_2$, $CaCl^+$, Mg^{2+}, $MgCl^+$, $MgOH^+$, Fe^{2+}, $FeCl^+$, $FeCl_2^0$, $FeOH^+$, $HFeO_2^-$, FeO^0, Fe^{3+}, $FeOH^{2+}$, FeO^+, $HFeO_2^0$, FeO_2^-	(32), updated Supcrt database
$NaSO_4^-$	(33)
HCl^0	(34)
H_2S^0, SO_2^0, H_2^0, O_2^0	(35)
$NaHS^0$, KHS^0, $NaHSO_4^0$	(6)
$Au(HS)_2^-$	(36)
$AuCl_2^-$	(8)
$Au(HS)S_3^-$	(6)
S_3^-	(37)
SiO_2^0, $Si_2O_4^0$, $HSiO_3^-$	(5)
$Fe(OH)_4^-$	(38)
$Fe(HSiO_3)^+$	(3)
$FeCl^{2+}$	Update DEW database
Al^{3+}, $AlOH_2^+$, $AlOH_3^0$, $AlOH_4^-$, $NaAl(OH)_4^0$	(39)
$AlO_2(SiO_2)^-$	(3)
Pure mineral phases and endmembers of solid solution models	
gold, hematite, magnetite, quartz, muscovite, sanidine orthopyroxene: enstatite, hedenbergite clinopyroxene: jadeite, diopside olivine: fayalite, forsterite garnet: pyrope, almandine	(28, 32)

Table S6. Geological and metal grade data of worldwide porphyry Cu-Au deposits from the literature. The compilation includes deposit name, geographic locations, magma affinity, Cu and Au tonnages and average grades. These data are retrieved from the United States Geological Survey (https://mrdata.usgs.gov/porcu/), Chiaradia (40) and references therein. Abbreviations: CA = calc-alkaline (up to medium-K calc-alkaline); K = high-K calc-alkaline to alkaline.

Deposit	Province	Latitude	Longitude	Magma	Ref.	Cu tonnage (Mt)	Au tonnage (t)	Cu average grade (wt.%)	Au average grade (ppm)
Agua Rica	Argentina	-27.37	-66.28	K	(41)	7.4	317	0.42	0.180
Aksug	Russia (Siberia)	53.43	96.67	CA	(42)	4.2	126	0.67	0.120
Aktogay	Kazakhstan	46.97	79.98	CA	(43)	12.5	92.8	0.37	0.031
Amacan	Philippines	7.33	126.15	CA	(42)	0.41	44	0.30	0.430
Ann Mason	US	38.96	-119.27	CA	(42)	3.8	56.25	0.33	0.030
Antapaccay	Peru (S.)	-14.96	-71.35	CA	(44)	3.2	70.8	0.74	0.150
Atlas	Philippines	10.37	123.83	CA	(43)	6.9	331	0.45	0.240
Bagdad	US (Arizona)	34.59	-113.21	CA	(42)	6.4	1.8	0.40	0.001
Bajo de la Alumbrera	Argentina	-27.33	-66.61	K	(43)	4.3	516	0.53	0.640
Batu Hijau	Indonesia	-8.97	116.87	CA	(43)	7.2	572	0.44	0.350
Bell	Canada	55.00	-126.23	CA	(42)	1.8	79.2	0.36	0.160
Berg	Canada	53.80	-127.44	K	(42)	1.85	11.72	0.40	0.050
Bethlehem	Canada	50.49	-121.00	CA	(42)	3	3.39	0.45	0.005
Bingham	US (Utah)	40.53	-112.15	K	(43)	28.5	1603	0.88	0.380
Boyongan	Philippines	9.55	125.49	CA	(45)	1.4	196.6	0.60	1.000

Brenda	Canada	49.88	-120.01	CA	(42)	0.36	2.95	0.16	0.013
Butte	US (Montana)	39.80	-115.15	CA	(43)	35.1	217	0.67	0.042
Cadia	Australia	-33.47	149.00	K	(43)	9.7	1517	0.32	0.750
Cananea	Mexico	30.95	-110.32	CA	(43)	30	82	0.45	0.035
Chaucha	Ecuador	-2.93	-79.42	CA	(46)	1.5	—	—	—
Chino/Sta Rita	US (N. Mexico)	32.79	-108.07	CA	(42)	14.2	169.7	0.20	—
Chuquicamata	Chile (N.)	-22.28	-68.90	CA	(42)	106	276.6	0.59	0.013
Cobre Panama	Panama	8.43	-81.50	CA	(42)	19.3	320.25	0.35	0.070
Copper Mt.	Canada	49.34	-120.56	K	(42)	1.7	118.6	0.47	0.170
Coroccohuayco	Peru (S.)	-14.95	-71.26	CA	(47)	2.43	51	1.57	0.330
Cu Basin	US (Nevada)	40.61	-117.04	CA	(42)	0.2	—	0.40	—
Cu Canyon	US (Nevada)	40.55	-117.13	CA	(42)	0.28	44	0.48	0.770
Cu Creek	US (Arizona)	32.75	-110.48	CA	(42)	0.6	—	0.75	—
Cuajone	Peru (S.)	-17.05	-70.71	CA	(43)	17.14	—	0.60	—
Dexing	China	29.02	117.73	CA	(42)	8.38	219	0.46	0.120
Dizon	Philippines	14.97	120.20	CA	(42)	0.67	174	0.36	0.930
El Abra	Chile (Central)	-21.92	-68.83	CA	(48)	8.8	—	—	—
El Salvador	Chile (N.)	-26.25	-69.55	CA	(43)	17.1	384	0.45	0.100
El Teniente	Chile (Central)	-34.09	-70.46	CA	(43)	130	103.7	0.62	0.005
Elatsite	Bulgaria	42.75	24.03	CA	(49)	1.4	91	0.39	0.260
Ely	Nevada (US)	39.26	-115.00	K	(42)	4.62	203.6	0.61	0.270

Escondida	Chile (N.)	-24.27	-69.07	CA	(43)	85.8	—	0.77	0.250
Esperanza	Chile	-22.97	-69.06	CA	(42)	7.3	229.6	0.51	0.160
Frieda River	PNG	-4.70	141.78	K	(43)	8.6	418	0.52	0.310
FSE Lepanto	Philippines	16.86	120.78	CA	(43)	5.48	973	0.50	1.420
Galore Creek	Canada	57.13	-131.45	K	(42)	9.3	636.6	0.55	0.310
Gibraltar	Canada	52.52	-122.29	CA	(42)	3.8	90.8	0.30	0.070
Golpu-Wafi	PNG	-6.88	146.45	K	(50)	4.9	302	1.00	0.700
Goonumbla	NSW Australia	-32.92	148.03	K	(42)	1.75	70	0.70	0.280
Gransile	BC (Canada)	54.95	-126.16	CA	(42)	0.7	25	0.43	0.120
Grasberg	Indonesia	-3.82	137.23	K	(43)	28.02	2604	0.60	0.640
Highmont	Canada	50.43	-120.92	CA	(42)	0.705	1.06	0.27	0.004
Huckleberry	Canada	53.68	-127.18	CA	(42)	0.831	4.1	0.48	0.025
Iron Mask	Canada	13.50	121.88	CA	(42)	0.02	0.8	1.47	0.670
Island Copper	Canada	50.60	-127.48	CA	(42)	1.5	71.6	0.41	0.190
Ithaca Peak	Arizona (US)	35.37	-114.15	CA	(42)	1.25	23.7	0.14	0.027
Junin	Ecuador	0.33	-78.58	CA	(46)	8.7	9.8	0.61	0.200
Kadjaran	Armenia	39.14	46.14	K	(42)	4.6	1105	0.27	0.650
Kalamatan	Philippines	7.59	126.07	CA	(42)	0.09	9.62	0.34	0.370
Kingking	Philippines	7.17	125.99	CA	(42)	2.9	230.2	0.39	0.432
La Granja	Peru (N.)	-6.36	-79.12	CA	(43)	19.52	128	0.56	0.040
La Verde	Mexico	19.08	-102.03	CA	(42)	0.77	9.7	0.70	0.088

Lobo	Chile	17.47	120.82	CA	(51)	9.6	128	—	—
Lone Star	Arizona	32.93	-109.60	CA	(43)	24.74	—	0.45	—
Lornex	Canada	50.45	-121.04	CA	(42)	2.19	3.08	0.43	0.006
Los Pelambres	Chile (Central)	-31.71	-70.50	CA	(43)	46	209	0.62	0.028
Mamut	Malaysia	6.03	116.47	K	(42)	0.94	98	0.48	0.500
Mangzong	Tibet (China)	17.77	121.23	K	(44)	0.2	1.4	0.34	0.020
Mapula	Philippines	7.35	126.02	CA	(42)	0.31	28.9	0.40	0.370
Minas Conga	Peru (N.)	-6.92	-78.36	CA	(43)	1.92	506	0.30	0.790
Mirador	Ecuador	-4.65	-78.90	CA	(42)	5	142.4	0.56	0.160
Moldova	Romania	44.74	21.70	CA	(42)	1.8	—	0.35	—
Morenci	Arizona	33.10	-109.36	CA	(43)	33.9	181.2	0.52	0.028
Morrison	Canada	55.19	-126.32	CA	(42)	0.7	36.6	0.39	0.200
Mt. Polley	Canada	52.55	-121.64	K	(42)	0.66	63.5	0.23	0.300
OK Tedi	PNG	-5.20	141.13	K	(43)	5.5	666	0.64	0.780
Oyu Tolgoi	Mongolia	43.00	106.87	K	(52)	37	1427	0.68	0.240
Pampa Escondida	Chile (N.)	-22.28	-68.90	CA	(43)	7.92	135.62	1.15	0.190
Panguna	PNG	-6.32	155.50	CA	(43)	6.6	810	0.47	0.570
Pebble	Alaska	59.90	-155.30	K	(43)	31.2	2478	0.42	0.330
Peschanka	Kamchatka	66.60	164.57	CA	(43)	7.9	455	0.51	0.420
Pima	Arizona	31.98	-111.07	CA	(43)	13.1	—	0.69	—

Potrerillos	Chile (N.)	-26.49	-69.42	CA	(43)	10.1	793	0.98	0.770
Qulong	Tibet (China)	29.60	91.58	K	(53)	8	—	0.52	—
Radomiro Tomic	Chile (N.)	-22.28	-68.90	CA	(43)	19.9	—	0.39	—
Ray	US (Arizona)	33.16	-110.98	CA	(43)	10.8	3.2	0.68	0.002
Recsk	Hungary	47.93	20.10	CA	(42)	4.6	196	0.66	0.280
Refugio	Chile	-27.55	-69.30	CA	(51)	0.22	190.1	0.03	1.020
Reko Diq	Pakistan	29.12	62.08	CA	(54)	24.2	1298	0.51	0.270
Rio Blanco	Chile (Central)	-24.40	-69.61	CA	(43)	100.4	244.7	0.40	0.276
Rosario	Chile (N.)	-20.96	-68.71	CA	(43)	25.49	31.08	0.82	0.700
San Manuel	Arizona	32.70	-110.68	CA	(42)	8	24	0.60	0.017
Santo Nino	Philippines	16.49	120.66	CA	(42)	0.6	57	0.35	0.200
Santo Tomas	Philippines	16.26	120.62	CA	(42)	1.7	314.3	0.38	0.700
Sar Cheshmeh	Iran	29.95	55.86	CA	(43)	8.9	92	1.20	0.270
Schaft Creek	Canada	57.36	-130.99	CA	(42)	3.48	250.7	0.25	0.180
Silver Bell	US (Arizona)	32.40	-111.50	CA	(42)	1.8	7	0.66	0.026
Sipilay	Philippines	9.82	122.45	CA	(42)	4.42	301	0.47	0.050
Skouries	Greece	40.47	23.70	K	(42)	2	267	0.35	0.470
Sungun	Iran	38.81	46.37	CA	(42)	3.8	—	0.66	—
Tagpura-Maangob	Philippines	7.54	126.10	CA	(42)	0.097	5.29	0.44	0.500
Tampakan	Philippines	6.48	125.05	CA	(43)	15	500	0.48	0.200

Tanamá	Puerto Rico	18.25	-66.82	CA	(42)	0.81	47.9	0.64	0.380
Taysan	Philippines	13.80	121.13	CA	(42)	2.1	87	0.31	0.300
Toki	Chile (N.)	-22.42	-68.95	CA	(43)	10.85	—	0.45	—
Valley Copper	Canada	50.49	-121.05	CA	(42)	5	8.14	0.43	0.006
Yandera	P. N. Guinea	-5.75	145.17	K	(42)	2.4	72.86	0.42	0.100
Yerington	US (Nevada)	38.98	-119.20	CA	(42)	3.5	42.7	0.51	0.046
Yulong	Tibet (China)	31.40	97.73	K	(44)	6.2	220.5	0.84	0.350
Zlatno	Slovakia	48.44	18.86	CA	(42)	0.2	—	0.50	—
Zijinshan	China	25.18	116.40	CA	(42)	1.7	50	0.49	0.140
Xiongcun	China	29.36	88.43	CA	(42)	3.3	239	0.30	0.220
Tuwu-Yandong	China	42.10	92.56	CA	(42)	3.2	99	0.49	0.150

SI References

1. M. Anenburg, H. S. C. O'Neill, Redox in magmas: comment on a recent treatment of the kaiserstuhl volcanics and some other misconceptions. *J. Petrol.* **60**, 1825-1832 (2019).
2. T. J. B. Holland, R. Powell, An improved and extended internally consistent thermodynamic dataset for phases of petrological interest, involving a new equation of state for solids. *J. Metamorph. Geol.* **29**, 333-383 (2011).
3. F. Huang, D. A. Sverjensky, Extended Deep Earth Water Model for predicting major element mantle metasomatism. *Geochim. Cosmochim. Acta* **254**, 192-230 (2019).
4. M. E. Galvez, C. E. Manning, J. A. D. Connolly, D. Rumble, The solubility of rocks in metamorphic fluids: A model for rock-dominated conditions to upper mantle pressure and temperature. *Earth Planet. Sci. Lett.* **430**, 486-498 (2015).
5. D. A. Sverjensky, B. Harrison, D. Azzolini, Water in the deep Earth: The dielectric constant and the solubilities of quartz and corundum to 60kb and 1200°C. *Geochim. Cosmochim. Acta* **129**, 125-145 (2014).
6. G. S. Pokrovski *et al.*, Sulfur radical species form gold deposits on Earth. *Proc. Nat. Acad. Sci.* **112**, 13484-13489 (2015).
7. K. Kouzmanov, G. S. Pokrovski, Hydrothermal Controls on Metal Distribution in Porphyry Cu (-Mo-Au) Systems. Society of Economic Geologists, Special Publication **16**, 573-618 (2012).
8. K. Rauchenstein-Martinek, T. Wagner, M. Wälle, C. A. Heinrich, Gold concentrations in metamorphic fluids: A LA-ICPMS study of fluid inclusions from the Alpine orogenic belt. *Chem. Geol.* **385**, 70-83 (2014).
9. S. Jégo, R. Dasgupta, Fluid-present melting of sulfide-bearing ocean-crust: Experimental constraints on the transport of sulfur from subducting slab to mantle wedge. *Geochim. Cosmochim. Acta* **110**, 106-134 (2013).
10. S. Jégo, R. Dasgupta, The fate of sulfur during fluid-present melting of subducting basaltic crust at variable oxygen fugacity. *J. Petrol.* **55**, 1019-1050 (2014).
11. Y. Li, A. Audétat, Partitioning of V, Mn, Co, Ni, Cu, Zn, As, Mo, Ag, Sn, Sb, W, Au, Pb, and Bi between sulfide phases and hydrous basanite melt at upper mantle conditions. *Earth Planet. Sci. Lett.* **355-356**, 327-340 (2012).
12. Y. Li, A. Audétat, Gold solubility and partitioning between sulfide liquid, monosulfide solid solution and hydrous mantle melts: Implications for the formation of Au-rich magmas and crust–mantle differentiation. *Geochim. Cosmochim. Acta* **118**, 247-262 (2013).
13. R. E. Botcharnikov *et al.*, Behavior of gold in a magma at sulfide-sulfate transition: Revisited. *Am. Mineral.* **98**, 1459-1464 (2013).
14. Z. Zajacz, P. A. Candela, P. M. Piccoli, M. Wälle, C. Sanchez-Valle, Gold and copper in volatile saturated mafic to intermediate magmas: Solubilities, partitioning, and implications for ore deposit formation. *Geochim. Cosmochim. Acta* **91**, 140-159 (2012).
15. M. E. Galvez, J. A. D. Connolly, C. E. Manning, Implications for metal and volatile cycles from the pH of subduction zone fluids. *Nature* **539**, 420-424 (2016).
16. T. Kawamoto *et al.*, Mantle wedge infiltrated with saline fluids from dehydration and decarbonation of subducting slab. *Proc. Nat. Acad. Sci.* **110**, 9663-9668 (2013).
17. P. J. Jugo, R. W. Luth, J. P. Richards, An experimental study of the sulfur content in basaltic melts saturated with immiscible sulfide or sulfate liquids at 1300°c and 1·0 gpa. *J. Petrol.* **46**, 783-798 (2005).
18. K. A. Kelley, T. Plank, J. Ludden, H. Staudigel, Composition of altered oceanic crust at ODP Sites 801 and 1149. *Geochem. Geophys. Geosyst.* **4**, 8910 (2003).
19. J. A. Padrón-Navarta, V. López Sánchez-Vizcaíno, C. J. Garrido, M. T. Gómez-Pugnaire, Metamorphic record of high-pressure dehydration of antigorite serpentinite to chlorite harzburgite in a subduction setting (Cerro del Almirez, Nevado–Filábride Complex, Southern Spain). *J. Petrol.* **52**, 2047-2078 (2011).
20. K. A. Evans, The redox budget of subduction zones. *Earth Sci. Rev.* **113**, 11-32 (2012).
21. V. J. M. Salters, A. Stracke, Composition of the depleted mantle. *Geochem. Geophys. Geosyst.* **5**, Q05B07 (2004).
22. D. Canil *et al.*, Ferric iron in peridotites and mantle oxidation states. *Earth Planet. Sci. Lett.*

123, 205-220 (1994).

23. E. C. R. Green *et al.*, Activity–composition relations for the calculation of partial melting equilibria in metabasic rocks. *J. Metamorph. Geol.* **34**, 845-869 (2016).
24. T. J. B. Holland, E. C. R. Green, R. Powell, Melting of peridotites through to granites: A simple thermodynamic model in the system KNCFMASHTOCr. *J. Petrol.* **59**, 881-900 (2018).
25. R. White, R. Powell, T. Holland, T. Johnson, E. Green, New mineral activity–composition relations for thermodynamic calculations in metapelitic systems. *J. Metamorph. Geol.* **32**, 261-286 (2014).
26. E. Green, T. Holland, R. Powell, An order-disorder model for omphacitic pyroxenes in the system jadeite-diopside-hedenbergite-acmite, with applications to eclogitic rocks. *Am. Mineral.* **92**, 1181-1189 (2007).
27. T. Holland, R. Powell, An internally consistent thermodynamic data set for phases of petrological interest. *J. Metamorph. Geol.* **16**, 309-343 (1998).
28. T. Holland, R. Powell, An improved and extended internally consistent thermodynamic dataset for phases of petrological interest, involving a new equation of state for solids. *J. Metamorph. Geol.* **29**, 333-383 (2011).
29. M. L. Fuhrman, D. H. Lindsley, Ternary-feldspar modeling and thermometry. *Am. Mineral.* **73**, 201-215 (1988).
30. H. J. Massonne, A. P. Willner, Phase relations and dehydration behaviour of psammopelite and mid-ocean ridge basalt at very-low-grade to low-grade metamorphic conditions. *Eur. J. Mineral.* **20**, 867-879 (2008).
31. J. A. D. Connolly, M. E. Galvez, Electrolytic fluid speciation by Gibbs energy minimization and implications for subduction zone mass transfer. *Earth Planet. Sci. Lett.* **501**, 90-102 (2018).
32. J. W. Johnson, E. H. Oelkers, H. C. Helgeson, SUPCRT92: A software package for calculating the standard molal thermodynamic properties of minerals, gases, aqueous species, and reactions from 1 to 5000 bar and 0 to 1000°C. *Comput. Geosci.* **18**, 899-947 (1992).
33. G. S. Pokrovski, J. Schott, A. S. Sergeyev, Experimental determination of the stability constants of $NaSO_4^-$ and $NaB(OH)_4^0$ in hydrothermal solutions using a new high-temperature sodium-selective glass electrode-Implications for boron isotopic fractionation. *Chem. Geol.* **124**, 253-265 (1995).
34. B. R. Tagirov, A. V. Zotov, N. N. Akinfiev, Experimental study of dissociation of HCl from 350 to 500°C and from 500 to 2500 bars: Thermodynamic properties of HCl^0(aq). *Geochim. Cosmochim. Acta* **61**, 4267-4280 (1997).
35. M. D. Schulte, E. L. Shock, R. H. Wood, The temperature dependence of the standard-state thermodynamic properties of aqueous nonelectrolytes. *Geochim. Cosmochim. Acta* **65**, 3919-3930 (2001).
36. G. S. Pokrovski, N. N. Akinfiev, A. Y. Borisova, A. V. Zotov, K. Kouzmanov, Gold speciation and transport in geological fluids: insights from experiments and physical-chemical modelling. *Geol. Soc. Lond. Spec. Publ.* **402**, 9-70 (2014).
37. G. S. Pokrovski, J. Dubessy, Stability and abundance of the trisulfur radical ion S_3^- in hydrothermal fluids. *Earth Planet. Sci. Lett.* **411**, 298-309 (2015).
38. I. I. Diakonov, J. Schott, F. Martin, J.-C. Harrichourry, J. Escalier, Iron(III) solubility and speciation in aqueous solutions. experimental study and modelling: part 1. hematite solubility from 60 to 300°C in NaOH–NaCl solutions and thermodynamic properties of Fe(OH)4−(aq). *Geochim. Cosmochim. Acta* **63**, 2247-2261 (1999).
39. B. Tagirov, J. Schott, Aluminum speciation in crustal fluids revisited. *Geochim. Cosmochim. Acta* **65**, 3965-3992 (2001).
40. M. Chiaradia, Gold endowments of porphyry deposits controlled by precipitation efficiency. *Nat. Commun.* **11**, 248 (2020).
41. M. R. Landtwing, E. D. Dillenbeck, M. H. Leake, C. A. Heinrich, Evolution of the breccia-hosted porphyry Cu-Mo-Au deposit at Agua Rica, Argentina: Progressive unroofing of a magmatic hydrothermal system. *Econ. Geol.* **97**, 1273-1292 (2002).
42. U.S. Geological Survey, “Porphyry copper deposits of the world” available at

http://mrdata.usgs.gov/porcu/ and references therein.

43. D. R. Cooke, P. Hollings, J. L. Walshe, Giant porphyry deposits: characteristics, distribution, and tectonic controls. *Econ. Geol.* **100**, 801-818 (2005).
44. Anonymous, http://www.portergeo.com.au/database and references therein.
45. D. P. Braxton *et al.*, From crucible to graben in 2.3 Ma: A high-resolution geochronological study of porphyry life cycles, Boyongan-Bayugo copper-gold deposits, Philippines. *Geology* **40**, 471-474 (2012).
46. P. Schütte, M. Chiaradia, B. Beate, Petrogenetic evolution of arc magmatism associated with Late Oligocene to Late Miocene porphyry-related ore deposits in Ecuador. *Econ. Geol.* **105**, 1243-1270 (2010).
47. C. Chelle-Michou, M. Chiaradia, P. Béguelin, A. Ulianov, Petrological evolution of the magmatic suite associated with the Coroccohuayco Cu(–Au–Fe) porphyry–skarn deposit, Peru. *J. Petrol.* **56**, 1829-1862 (2015).
48. K. J. Correa, O. M. Rabbia, L. B. Hernández, D. Selby, M. Astengo, The timing of magmatism and ore formation in the El Abra porphyry copper deposit, northern chile: Implications for long-lived multiple-event magmatic-hydrothermal porphyry systems. *Econ. Geol.* **111**, 1-28 (2016).
49. A. Von Quadt *et al.*, The Elatsite porphyry copper deposit in the Panagyurishte ore district, Srednogorie zone, Bulgaria: U-Pb zircon geochronology and isotope-geochemical investigations of magmatism and ore genesis. *Geol. Soc. Lond. Spec. Publ.* **204**, 119-135 (2002).
50. M. L. Rinne *et al.*, Geology and geochronology of the Golpu porphyry and Wafi epithermal deposit, Morobe Province, Papua New Guinea. *Econ. Geol.* **113**, 271-294 (2018).
51. S. M. Kay, C. Mpodozis, A. Tittler, P. Cornejo, Tertiary magmatic evolution of the Maricunga Mineral Belt in Chile. *Int. Geol. Rev.* **36**, 1079-1112 (1994).
52. A. J. Wainwright, R. M. Tosdal, J. L. Wooden, F. K. Mazdab, R. M. Friedman, U–Pb (zircon) and geochemical constraints on the age, origin, and evolution of Paleozoic arc magmas in the Oyu Tolgoi porphyry Cu–Au district, southern Mongolia. *Gondwana Res.* **19**, 764-787 (2011).
53. Y. B. Hu *et al.*, The formation of Qulong adakites and their relationship with porphyry copper deposit: Geochemical constraints. *Lithos* **220-223**, 60-80 (2015).
54. A. Razique, R. M. Tosdal, R. A. Creaser, Temporal evolution of the western porphyry Cu-Au systems at Reko Diq, Balochistan, Western Pakistan. *Econ. Geol.* **109**, 2003-2021 (2014).